LETTER

Conformational transitions of the serotonin 5–HT₃ receptor

Lucie Polovinkin[1], Ghérici Hassaine[2], Jonathan Perot[1], Emmanuelle Neumann[1], Anders A. Jensen[3], Solène N. Lefebvre[4], Pierre-Jean Corringer[4], Jacques Neyton[1]*, Christophe Chipot[5,6,7], Francois Dehez[5,6], Guy Schoehn[1] & Hugues Nury[1]*

The serotonin 5-HT₃ receptor is a pentameric ligand-gated ion channel (pLGIC). It belongs to a large family of receptors that function as allosteric signal transducers across the plasma membrane[1,2]; upon binding of neurotransmitter molecules to extracellular sites, the receptors undergo complex conformational transitions that result in transient opening of a pore permeable to ions. 5-HT₃ receptors are therapeutic targets for emesis and nausea, irritable bowel syndrome and depression[3]. In spite of several reported pLGIC structures[4–8], no clear unifying view has emerged on the conformational transitions involved in channel gating. Here we report four cryo-electron microscopy structures of the full-length mouse 5-HT₃ receptor in complex with the anti-emetic drug tropisetron, with serotonin, and with serotonin and a positive allosteric modulator, at resolutions ranging from 3.2 Å to 4.5 Å. The tropisetron-bound structure resembles those obtained with an inhibitory nanobody[5] or without ligand[9]. The other structures include an 'open' state and two ligand-bound states. We present computational insights into the dynamics of the structures, their pore hydration and free-energy profiles, and characterize movements at the gate level and cation accessibility in the pore. Together, these data deepen our understanding of the gating mechanism of pLGICs and capture ligand binding in unprecedented detail.

A decade after the structure of the *Torpedo marmorata* nicotinic acetylcholine receptor[10] (nAChR), the set of known pLGIC structures is rapidly expanding and reflects the diversity of this protein family. The structures share a conserved architecture, in which subunits are arranged around a central five-fold pseudo-symmetry axis. Together they have clarified details of ligand binding, selectivity and allosteric modulation. They have also revealed a complex landscape of conformations, raising questions of how to relate structures to the wealth of data that established the existence of multiple agonist-bound pre-active intermediate states[11–13], of distinct open states[14] and of multiple desensitized states[15].

Mouse homomeric 5-HT₃ₐ receptors, with their entire intracellular domain (ICD), were solubilized with the detergent C12E9 and purified. We first performed cryo-electron microscopy (cryo-EM) in the presence of the potent antagonist tropisetron, and obtained a 4.5 Å structure (Fig. 1b, Extended Data Figs. 1, 2, Extended Data Table 1), hereafter referred to as T. T is globally similar to the structure previously solved by X-ray crystallography[5] (root mean square deviation (r.m.s.d.) of 0.6 Å), the pore of which was shown by molecular dynamics to be occluded[16]. Tropisetron fits in a peanut-shaped density present in the neurotransmitter pocket (Extended Data Fig. 3d–f). The ICD contains a region of about 60 residues, which is averaged out (also in the other reconstructions, see below) because of its intrinsic flexibility[1,2]. T resembles the 4.5 Å cryo-EM structure of the apo 5-HT₃ receptor[9] (r.m.s.d. of 1.15 Å), with small differences in the lipid-exposed helices M3, MX and M4.

We then sought to identify agonist-elicited conformations of the 5-HT₃ receptor, and performed cryo-EM imaging in the presence of serotonin. A first reconstruction presented heterogeneity in the membrane domain. Further focused 3D classification allowed two subsets of particles to be separated, which yielded reconstructions at 4.2 Å and 4.1 Å resolution, corresponding to two different conformations (Fig. 1b, Extended Data Fig. 4). The maps offer a variable level of information: most side chains in the extracellular domain are resolved, whereas some parts of the transmembrane domain (TMD) do not have side-chain information and some have limited information in the main chain position (Extended Data Figs. 4c, 5), reflecting the receptor dynamics. In the two refined structures, the extracellular domains (ECDs) have undergone an equivalent transition from the T state and serotonin could be modelled in the neurotransmitter site, whereas the TMDs differed markedly (Fig. 2, Extended Data Fig. 6). We call the first structure I1 for intermediate 1 and the second structure F for full, on the basis of the extent of movements compared to the inhibited state. I1 exhibits only limited displacements in the upper part of M1 and M2, and a rearrangement of the M2–M3 loop (Supplementary Video 1). F is characterized by a pronounced reorganization of the transmembrane helices, which can be described by a rigid-body movement of the four-helix bundle coupled to a rearrangement of M4 (and of M3 to a lesser extent) sliding along M1 and M2 (Supplementary Videos 2, 3). F also features a very dynamic ICD, beyond the intrinsically disordered region, in which model building was not possible even though the data showed incomplete densities for MX and M4 (Extended Data Fig. 4a–c).

Finally, we collected a dataset in the presence of serotonin and trans-3-(4-methoxyphenyl)-N-(pentan-3-yl)acrylamide (TMPPAA, a compound exhibiting agonist and positive allosteric modulator activity on the human receptor[17]), a combination that yields weakly desensitizing currents (Extended Data Fig. 1f). From this dataset, we reconstructed a 3.2 Å resolution structure (Extended Data Fig. 2d–g), which provides non-ambiguous side-chain information for nearly the entire receptor. The refined structure has an ECD conformation essentially equivalent to that of I1 and F. The membrane domain is similar to that of I1, albeit with a slightly more expanded top section and pore (Fig. 2). We call this structure I2 for intermediate 2.

Serotonin can be unambiguously positioned in the neurotransmitter site of I2. It fits tightly within its binding pocket (Extended Data Fig. 3a–c) in an orientation consistent with functional and binding studies[1]. Surrounded by obligatory aromatic residues (F199 and Y207 on the principal side, Y126 and W63 on the complementary side), it is positioned to form a cation-π interaction with W156 and hydrogen bonds with the main chain of S155 and Y64. The C loop is positioned moderately inward relative to the inhibited conformations, its position locked by a salt bridge between D202 and R65. A hallmark of allosteric activation is the subunit–subunit rearrangement (Extended Data Fig. 3d), which affects the site volume and geometry.

[1]CNRS, Université Grenoble Alpes, CEA, IBS, Grenoble, France. [2]Theranyx, Marseille, France. [3]Department of Drug Design and Pharmacology, Faculty of Health and Medical Sciences, University of Copenhagen, Copenhagen, Denmark. [4]Channel Receptors Unit, CNRS UMR 3571, Institut Pasteur, Paris, France. [5]Université de Lorraine, CNRS, LPCT, Nancy, France. [6]Laboratoire International Associé CNRS and University of Illinois at Urbana-Champaign, Vandoeuvre-les-Nancy, France. [7]Department of Physics, University of Illinois at Urbana-Champaign, Urbana, IL, USA. *e-mail: jacques.neyton@ibs.fr; hugues.nury@ibs.fr
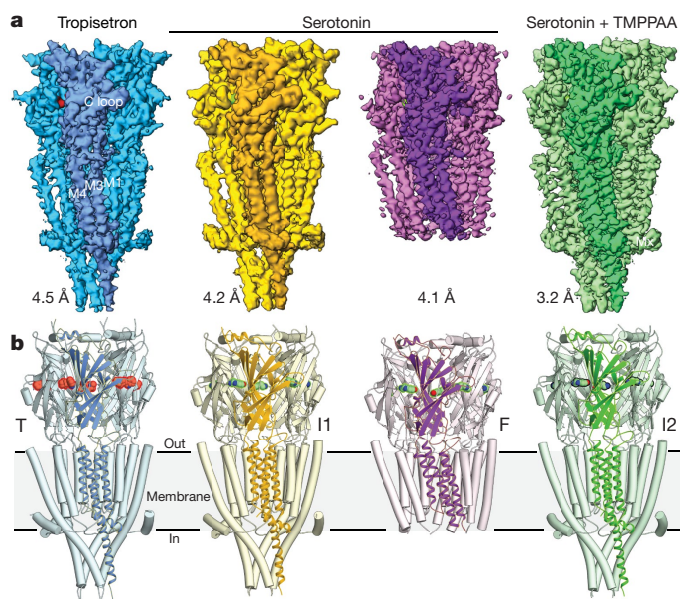
Fig. 1 | Three-dimensional reconstructions and structures of homomeric 5-HT₃ₐ receptor. a, b, Reconstructions (**a**) and structures (**b**) for: the tropisetron dataset (protein in blue and ligand in red), the serotonin and Ca²⁺ dataset (I1 in yellow, F in purple and ligand in green), and the serotonin and TMPPAA dataset (I2 and ligand in green). Resolutions are shown according to the Fourier shell coefficient 0.143 criterion.

TMPPAA has previously been proposed to bind to an allosteric site in the TMD[17], but there is no clearly interpretable density in our data to model the compound. We tested TMPPAA agonist activity on a set of around 45 single-point mutants of the human receptor, which collectively reveal that the drug binds between M4, M1 and M3 into an intra-subunit cavity skirted by lipids of the outer leaflet in the upper part of the TMD (Extended Data Fig. 7, Supplementary Table 1), where endogenous steroids bind to nAChRs[18]. More generally, several allosteric druggable sites have been identified in pLGICs, which bind diverse compounds including general anaesthetics such as propofol and flavourings such as citral or eucalyptol[3]. Allosteric sites in the 5-HT₃ receptor change in both shape and volume during transitions (Extended Data Figs. 3i, 7a).

At the ECD–TMD interface, a set of conserved residues that are essential for gating[19] form a structural motif that is common to all pLGIC structures, the location of which may correlate with the state of the channel[5]. This motif consists of charged residues (E53, D145, E186 and R218) sandwiched between conserved aromatic residues: W187 at the top and the 142-FPF-144 motif of the Cys loop, plus Y223 at the bottom (Extended Data Fig. 8). The FPF motif itself penetrates the transmembrane domain similar to a wedge; its position differs in each conformation. When superimposing structures on a TMD subunit, the wedge lies close to M2 in the tropisetron-bound structure and moves towards M4–M1 in the I1, I2 and F structures (which is possible because the conserved P230 allows the upper M1 to kink or straighten). A marked downward concerted movement of the wedge and of the β8–β9 loop (containing E186 and W187) occurs in the F structure, pushing on the M2–M3 loop, and may be responsible for the marked reorganization of the TMD observed in that state.

pLGIC pores are lined with side chains of residues from the five M2 helices. In direct agreement with results from substituted cysteine accessibility mutagenesis[1] (SCAM), our structures show that in all conformations, positions −1′, 2′, 6′, 9′, 13′, 16′, 17′ and 20′ of the M2 α-helix are exposed to the pore lumen (Fig. 3a). Positions 12′ and 15′, which are also accessible in SCAM, are partly exposed to solvent on the rear of the M2 helices. Superimposition of a single M2 helix underscores its flexibility at both ends; superimposition of the five M2 helices highlights the crucial role of movements of the hydrophobic

side chain at the 9′ position (Fig. 3b, c). Minimum pore diameter is often a key element in the assignment of experimental structures to physiological states. Pore profiles are compatible with closed hydrophobic gates (rings at positions 9′, 13′, 16′ and 17′) in the T and I1 structures, with an open channel in the F structure, whereas the I2 structure presents an intermediate profile. However, pore profiles are influenced by the resolution, symmetry and rotameric state of the side chains pointing into the pore lumen. Some positions, such as the key negative charge in −1′ are often poorly resolved in density maps, and are known to adopt alternate conformations[8,20]. Moreover, pore profiles are not informative about hydrophobicity, wetting or dynamics, which have key roles in permeability[21,22]. We performed molecular dynamics simulations to better characterize permeation. In the microsecond-long trajectories starting from the inhibited X-ray structure or from I1, no water or ions cross the pore, and the hydrophobic 9′, 13′ and 16′ rings establish a de-wetted hydrophobic gate that is tighter than in the starting structures (Fig. 3d, Extended Data Fig. 9). By sharp contrast, a simulation starting from F features an open pore that is accessible to ions and water throughout the trajectory (Supplementary Video 4). During the initial part of the simulations starting from I2, when the Cα atoms are positionally restrained, wetting and de-wetting events of the pore occur as if its conformation were on the open–closed verge (Extended Data Fig. 9). Wetting is linked to the presence of transiently hydrated grooves at the back of M2 helices, down to the polar residues Y11′–S12′, affecting the electrostatic landscape inside the pore. Wetting also correlates with rotation of L9′ out of the pore lumen. Once the geometric restraints are removed, the I2 pore relaxes to a closed conformation similar to that observed in the I1 trajectory. The absence of TMPPAA in the simulation may rationalize the closure. Potentials of mean force for the translocation of a K⁺ ion reveal an insurmountable 12 kcal mol⁻¹ barrier in the case of I1 (representative of closed hydrophobic gate conformations), and an essentially flat free-energy landscape in the case of F (Fig. 3e).

We asked whether the structures could be assigned to physiological states. T and F are straightforward to assign, whereas I1 and I2 are less so. T typifies an inhibited state, with resting-like ECD stabilized by tropisetron, and a closed pore, resembling the apo state. F represents an open state, with an activated ECD with bound serotonin, an activated TMD and a wide open pore. Two assignments are possible for the closely related I1 and I2 conformations (Fig. 4a). In a first scheme, I1 exemplifies a serotonin-bound, pre-active closed state, in which the ECD and the ECD–TMD interface—but not the TMD—have undergone a transition. This is consistent with single-channel analysis of the 5-HT₃ receptor, which yields kinetic models in which opening can occur from a ligand-bound pre-active state[14]. In a second scheme, I1 represents a closed desensitized state that occurs downstream from the open state. In both schemes, I2 is best described as in a state close to I1 (that is, close to either pre-active or desensitized) wherein the slightly wider pore promotes wetting, which could enable ion passage or merely favour the switch to a fully open state, consistent with TMPPAA-induced modulation.

A distinctive feature of the second scheme is that the activation gate, consisting of rings of hydrophobic residues in the upper pore, would open in the active state and close in the desensitized state. This implies a marked movement of the upper pore during desensitization, and no ion access from the extracellular compartment to the lower pore in the desensitized state. Functional experiments on anionic receptors indicate that they have distinct activation and desensitization gates, the latter being located at the cytoplasmic end of the pore[23]. Moreover, structures of the GABAₐ receptor β3 homopentamer and of the α4β2 nAChR, with pores constricted at positions −2′ and −1′, have been assigned to desensitized states[6,8]. These receptors, however, were engineered close to the constriction, a feature that can alter desensitization in 5-HT₃ receptors[24].

To challenge the two schemes, we measured the movement of the gate region and the accessibility of the pore to organic cations. First, we
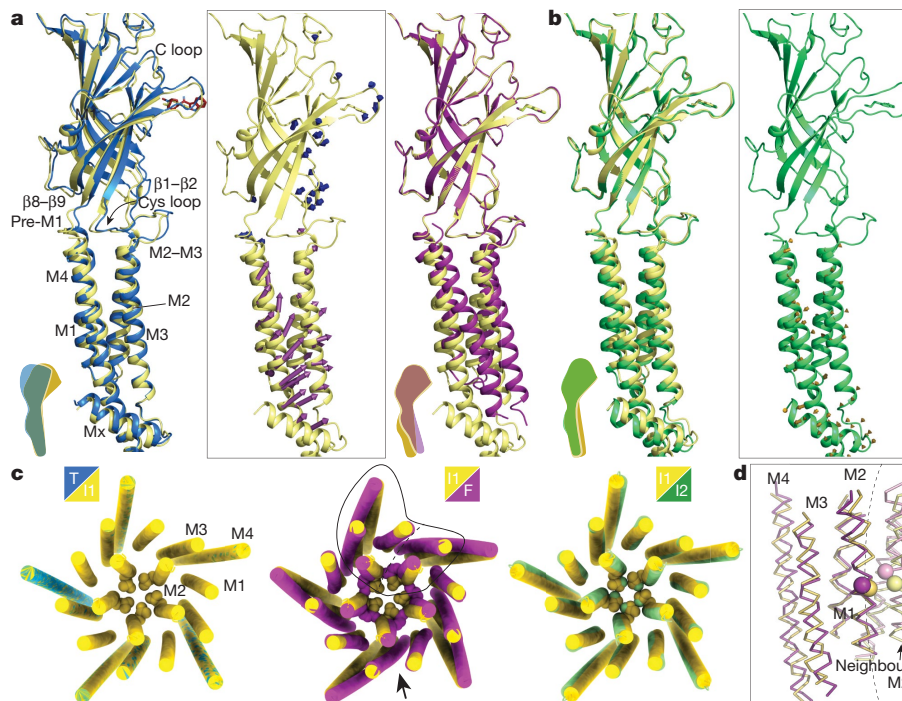
Fig. 2 | Transitions between the tropisetron-bound, the serotonin-bound, and the serotonin and TMPPA-bound states. a, View parallel to the membrane of one subunit of the serotonin-bound conformation I1 (yellow) overlaid with the tropisetron-bound conformation (blue, TMD superposition, left) or with the serotonin-bound conformation F (purple, ECD superposition, right). Inset, vectors indicate the local amplitude of movements, sampled on C_α atoms (T to I1 in blue, I1 to F in purple). **b**, Overlay of the I1 (yellow) and the serotonin and TMPPAA-bound I2 (green) conformations (left); vector representations of the I1 to I2 transition (ECD superposition). **c**, Pairwise overlays of the

TMD illustrating transitions at the quaternary level. Structures were superimposed on the ECD pentamer. L9′ (L260) residues are shown as spheres. The line and arrow on the middle overlay indicate the region depicted in **d** and the orientation of the view, respectively. **d**, Tertiary reorganization within a subunit TMD. Overlay in ribbon representation of I2 and F with L260 C_α as spheres (TMD superposition within a single subunit). Note the vertical shift of M3–M4 relative to M1–M2, distortions on the extracellular halves of M1–M2, and interface re-arrangement with the neighbouring subunit helices (on the right of the dotted line).

used voltage-clamp fluorometry (VCF) to probe the local conformational changes in the upper pore at the 19′ position[25,26] (Extended Data Fig. 10). We labelled S19′C mutants, expressed at the surface of *Xenopus*

laevis oocytes, with 5-carboxytetramethylrhodamine methanethiosulfonate (MTS-TAMRA). Transient stimulation with serotonin elicited simultaneous changes in current and fluorescence with parallel rise
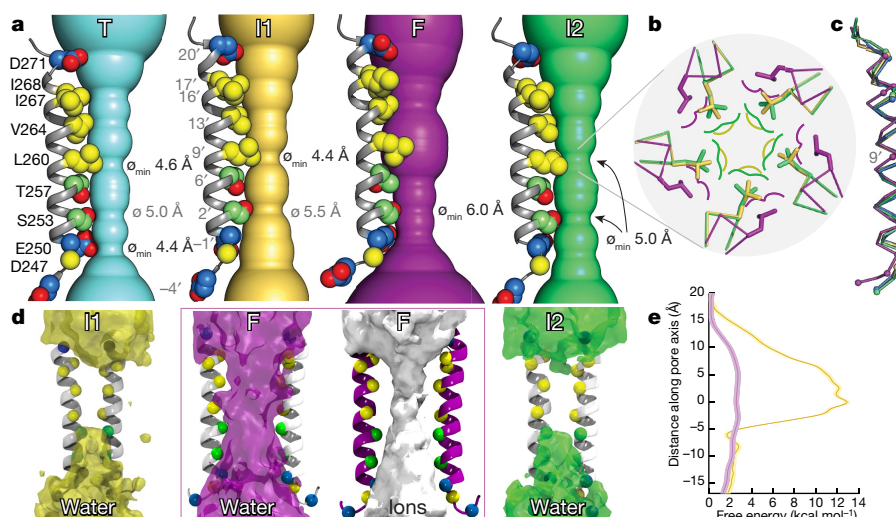
Fig. 3 | Geometry, wetting and energy landscape of the transmembrane pore. a, Static pore geometry; the accessible pathway through the pore is represented as a solid surface for each structure. Diameters ($\varnothing$) of the constriction zones are noted. One M2 helix is depicted as cartoon with pore-exposed side chains as spheres (polar in green, hydrophobic in yellow, charged in blue). The view is parallel to the plane of the membrane. **b**, Zoom on the hydrophobic gate constriction, formed at the level of L260 (sticks), which has a small movement backward in the I2 state and rotates

outwards in the F state. Coloured lines indicate molecular surfaces. The view is perpendicular to the membrane plane. **c**, Superposition of one M2 helix in the four conformations. **d**, Water densities of the pore region during the unrestrained part of simulations. Densities are depicted as transparent surfaces at the same contouring level. The density for K^+ ions is also included for the F trajectory featuring an open pore. **e**, Potentials of mean force of K^+ ions as a function of the position along the pore axis.
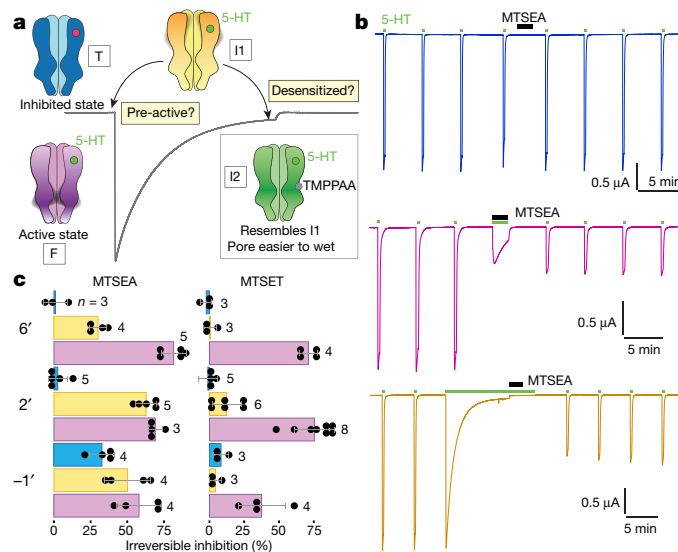
Fig. 4 | Putative molecular mechanisms of operation. a, T (blue) represents an inhibited state, stabilized by tropisetron (red circle). I1 (yellow) represents either a closed pre-active serotonin-bound (green circle) state or a desensitized state. F (purple) represents an open active state. The grey line illustrates the electrical response to serotonin recorded in an oocyte expressing 5-HT$_{3A}$ receptors. **b**, Recordings of MTSEA (1mM) modification on serotonin-evoked current in the S2′C mutant. MTSEA is applied in the resting (blue), the desensitized (orange), or active (purple) state. The protocol includes 10-s test serotonin applications before and after 2-min MTSEA modification. **c**, Changes in current after MTSEA (1 mM) or MTSET (1 mM) modification, for −1′C, S2′C and T6′C mutants, in the resting (blue), active (purple) or desensitized (yellow) state.

and decay, whereas prolonged (7-min) exposure to serotonin resulted in similar signals at the onset, followed by a slow decay for the current signal without a change in fluorescence. Both signals returned to baseline when serotonin was removed. The VCF results argue against the second scheme, because the probe environment changes upon activation but not during desensitization. Second, we performed SCAM in the resting (absence of ligand), open (during transient serotonin application) and desensitized (after prolonged serotonin application) states (Fig. 4b). MTSEA (2-aminoethyl methanethiosulfonate) and MTSET (2-2-(trimethylammonium)ethyl methanethiosulfonate) are organic cations that react with free cysteines through their methanethiosulfonate moiety. The aminoethyl head group of MTSEA is small, which enables it to access narrow spaces. MTSEA is, however, also known to cross membranes in its uncharged form. Application of 1 mM extracellular MTSEA in the resting state yielded no modification of currents in T6′C and S2′C mutants but inhibited currents (by 32%) in E1′C mutants (Fig. 4c). In the resting state, the compound can probably access position −1′ from the internal compartment, but it is unable to access the 2′ or 6′ positions. Similar applications in the open state produced irreversible inhibitions at 6′, 2′ and −1′ positions (82%, 69% and 58%, respectively). MTSEA can therefore reach 6′ and 2′ from the extracellular compartment in the open state, consistent with previous studies[1] and with the opening of the activation gate in F. Applications of extracellular MTSEA in the desensitized state also produced irreversible inhibitions at 6′, 2′ and −1′ positions (30%, 63% and 50%, respectively). From these results, we infer that positions 6′ and 2′, located below the hydrophobic gate seen in T and I1, are accessible from the extracellular side in the desensitized state. No conclusions can be drawn for position −1′, as its labelling in the resting state precludes further interpretation. The results suggest that the activation gate is open in the desensitized conformation(s). MTSET possesses a bulkier trimethylammonium headgroup and cannot cross membranes. We observed that MTSET labels cysteine mutants at 6′, 2′ and −1′ positions when applied in the open state (71%, 75% and 46%, respectively). Application of MTSET in the desensitized state yielded a small variable inhibition at 2′ (12 ± 10%) and none at 6′, indicating that these positions are more accessible for MTSEA than for the bulkier MTSET. On the basis of these results, we favour the scheme in which I1 is assigned to a pre-active state. Nevertheless, desensitization is a complex process involving

several distinct states[15], and we cannot rule out the possibility that I1 represents a desensitized state.

The challenge of matching structures to states without ambiguity transcends the present study and pertains to the whole field of pLGIC structures[2,27,28]. This challenge arises from diverse factors: limited resolution, putative influence of detergent, crystal packing and receptor engineering, and the possibility that ensembles of multiple related conformations are necessary to properly depict a physiological state. Bearing in mind the ambiguities on state assignment, we compared the 5-HT$_3$ transitions to those observed for the *Gloeobacter violaceus* receptor (GLIC)[4], the worm glutamate-gated receptor (GluCl)[29] and the glycine α1 receptor (GlyR)[7]. Common agonist-induced features emerge, such as a global twist, quaternary reorganization of the ECD, rearrangement of the interface between domains involving the conserved sandwich motif, and local movements of the upper TMD. Differences also appear: the extent of TMD reorganization seen in F, with M4 sliding on other helices, is not observed in the other receptors; the ECD reorganization is well-described as 'un-blooming'[4] for GLIC and GluCl, but not for the 5-HT$_3$ and glycine receptors. The open pore of F is wider than that of GLIC and narrower than that of GlyR. Bacterial, animal anionic and animal cationic channels may have evolved distinct sets of conformations for a given physiological state, as they belong to separate branches of the pLGIC family. Our 5-HT$_3$ receptor structures highlight several transitions in the cationic branch. They also contribute to knowledge on other important aspects of pLGIC research that are only alluded to in this report, such as the role of M4 in gating, the pharmacology of allosteric sites and ICD dynamics. Further work with better resolution, structures of mutant receptors and structures of receptors in complex with other ligands will complement and increase mechanistic insights, but knowledge of this area may nevertheless remain incomplete until kinetic structural experiments come of age.

Online content

Any methods, additional references, Nature Research reporting summaries, source data, statements of data availability and associated accession codes are available at https://doi.org/10.1038/s41586-018-0672-3.

1. Thompson, A. J., Lester, H. A. & Lummis, S. C. R. The structural basis of function in Cys-loop receptors. *Q. Rev. Biophys.* **43**, 449–499 (2010).
2. Nemecz, À., Prevost, M. S., Menny, A. & Corringer, P.-J. Emerging molecular mechanisms of signal transduction in pentameric ligand-gated ion channels. *Neuron* **90**, 452–470 (2016).
3. Sparling, B. A. & DiMauro, E. F. Progress in the discovery of small molecule modulators of the Cys-loop superfamily receptors. *Bioorg. Med. Chem. Lett.* **27**, 3207–3218 (2017).
4. Sauguet, L. et al. Crystal structures of a pentameric ligand-gated ion channel provide a mechanism for activation. *Proc. Natl Acad. Sci. USA.* **111**, 966–971 (2014).
5. Hassaïne, G. et al. X-ray structure of the mouse serotonin 5-HT₃ receptor. *Nature* **512**, 276–281 (2014).
6. Miller, P. S. & Aricescu, A. R. Crystal structure of a human GABA_A receptor. *Nature* **512**, 270–275 (2014).
7. Du, J., Lü, W., Wu, S., Cheng, Y. & Gouaux, E. Glycine receptor mechanism elucidated by electron cryo-microscopy. *Nature* **526**, 224–229 (2015).
8. Morales-Perez, C. L., Noviello, C. M. & Hibbs, R. E. X-ray structure of the human α4β2 nicotinic receptor. *Nature* **538**, 411–415 (2016).
9. Basak, S. et al. Cryo-EM structure of 5-HT₃A receptor in its resting conformation. *Nat. Commun.* **9**, 514 (2018).
10. Unwin, N. Refined structure of the nicotinic acetylcholine receptor at 4 Å resolution. *J. Mol. Biol.* **346**, 967–989 (2005).
11. Mukhtasimova, N., Lee, W., Wang, H. & Sine, S. Detection and trapping of intermediate states priming nicotinic receptor channel opening. *Nature* **459**, 451–454 (2009).
12. Lape, R., Colquhoun, D. & Sivilotti, L. G. On the nature of partial agonism in the nicotinic receptor superfamily. *Nature* **454**, 722–727 (2008).
13. Menny, A. et al. Identification of a pre-active conformation of a pentameric channel receptor. *eLife* **6**, e23955 (2017).
14. Corradi, J., Gumilar, F. & Bouzat, C. Single-channel kinetic analysis for activation and desensitization of homomeric 5-HT₃A receptors. *Biophys. J.* **97**, 1335–1345 (2009).
15. Sakmann, B., Patlak, J. & Neher, E. Single acetylcholine-activated channels show burst-kinetics in presence of desensitizing concentrations of agonist. *Nature* **286**, 71–73 (1980).
16. Trick, J. L. et al. Functional annotation of ion channel structures by molecular simulation. *Structure* **6**, 2207–2216 (2016).
17. Gasiorek, A. et al. Delineation of the functional properties and the mechanism of action of TMPPAA, an allosteric agonist and positive allosteric modulator of 5-HT₃ receptors. *Biochem. Pharmacol.* **110–111**, 92–108 (2016).
18. Jin, X. & Steinbach, J. H. A portable site: a binding element for 17β-estradiol can be placed on any subunit of a nicotinic α4β2 receptor. *J. Neurosci.* **31**, 5045–5054 (2011).
19. Mukhtasimova, N. & Sine, S. M. Nicotinic receptor transduction zone: invariant arginine couples to multiple electron-rich residues. *Biophys. J.* **104**, 355–367 (2013).
20. Cymes, G. D. & Grosman, C. The unanticipated complexity of the selectivity-filter glutamates of nicotinic receptors. *Nat. Chem. Biol.* **8**, 975–981 (2012).
21. Zhu, F. & Hummer, G. Drying transition in the hydrophobic gate of the GLIC channel blocks ion conduction. *Biophys. J.* **103**, 219–227 (2012).
22. Aryal, P., Sansom, M. S. P. & Tucker, S. J. Hydrophobic gating in ion channels. *J. Mol. Biol.* **427**, 121–130 (2015).
23. Gielen, M., Thomas, P. & Smart, T. G. The desensitization gate of inhibitory Cys-loop receptors. *Nat. Commun.* **6**, 6829 (2015).
24. McKinnon, N. K., Bali, M. & Akabas, M. H. Length and amino acid sequence of peptides substituted for the 5-HT₃A receptor M3M4 loop may affect channel expression and desensitization. *PLoS ONE* **7**, e35563 (2012).
25. Pless, S. A., Dibas, M. I., Lester, H. A. & Lynch, J. W. Conformational variability of the glycine receptor M2 domain in response to activation by different agonists. *J. Biol. Chem.* **282**, 36057–36067 (2007).
26. Dahan, D. S. et al. A fluorophore attached to nicotinic acetylcholine receptor βM2 detects productive binding of agonist to the αδ site. *Proc. Natl Acad. Sci. USA* **101**, 10195–10200 (2004).
27. daCosta, C. J. B. & Baenziger, J. E. Gating of pentameric ligand-gated ion channels: structural insights and ambiguities. *Structure* **21**, 1271–1283 (2013).
28. Gonzalez-Gutierrez, G., Wang, Y., Cymes, G. D., Tajkhorshid, E. & Grosman, C. Chasing the open-state structure of pentameric ligand-gated ion channels. *J. Gen. Physiol.* **149**, 1119–1138 (2017).
29. Hibbs, R. E. & Gouaux, E. Principles of activation and permeation in an anion-selective Cys-loop receptor. *Nature* **474**, 54–60 (2011).

Author contributions L.P., J.P. and G.H. performed sample preparation. L.P., H.N, E.N. and G.S. optimized and collected microscopy data. L.P. and H.N. built the models. F.D. and C.C. conducted molecular dynamics simulations. J.N. performed electrophysiology experiments. S.N.L. and P.-J.C. performed VCF experiments. A.A.J. performed FLIPR experiments. All authors extensively discussed the data, H.N. and J.N. wrote the manuscript with inputs from all authors.

METHODS

No statistical methods were used to predetermine sample size. The experiments were not randomized. The investigators were not blinded to allocation during experiments and outcome assessment.

Protein expression. The wild-type mouse 5-HT$_{3A}$ receptor was expressed in a stable, inducible cell line derived from HEK T-REx 293 cells (Thermo Fisher), as previously described[5,30,31]. The cells were cultured in suspension in flasks in an orbital incubator (typical culture size, 5 l). The protein expression was induced when cells reached 2×10^6 cells/ml. Valproic acid was added one day later and cells were cultured for one more day. Cells were then pelleted by low-speed centrifugation, frozen and stored at −80°C.

Protein purification. In a typical purification batch, 20 g of cells were resuspended in buffer A (10 mM HEPES pH 7.4, 1 mM EDTA, antiprotease cocktail; 10 ml buffer per gram of cells) mechanically lysed (Ultraturrax T20, 6 × 30 s) and membranes were collected by ultracentrifugation (100,000g for 1 h). All steps were carried out at 4 °C. Membranes were resuspended in buffer B (50 mM Tris pH 8, 500 mM NaCl, antiprotease cocktail, 25 ml buffer per gram of membrane) and the solution was supplemented with 0.15% of C12E9 for solubilisation using gentle stirring (1.5 h). The insoluble material was removed by ultracentrifugation (100,000g for 45 min). Solubilized proteins were purified by affinity chromatography using gravity flow Strep-Tactin resin (IBA, typically 25 ml resin), eluted in buffer C (50 mM Tris pH 7.5, 125 mM NaCl, 0.01% C12E9) and concentrated to ~0.5 mg/ml using Millipore 100-kDa cut-off filters. The purification tag was cleaved, and carbohydrates were digested by addition of 0.04 mg TEV protease and 0.1 mg PNGase F per 1 mg protein with gentle stirring overnight. The protein was further concentrated and then applied to a Superose 6 column (GE healthcare) equilibrated in buffer C.

Electron microscopy. The most homogeneous fractions of 5-HT$_3$ receptor following size-exclusion chromatography were concentrated to ~1.5 mg/ml (in the best cases, no concentration was required). The sample was mixed with lipids (0.01% phosphatidic acid, 0.01% cholesterol hemisuccinate, 0.01% brain phosphatidylcholine; Avanti Polar Lipids) and ligands: 2 mM tropisetron (Tocris), or 50 μM serotonin and 2 mM calcium (conditions known to promote fast desensitization[32,33]); or 30 μM serotonin and 100 mM TMPPAA (Sigma-Aldrich). Samples were incubated for 10–30 min on ice. 3.5 μl were deposited on a glow-discharged (30 mA, 50 s) Quantifoil copper-rhodium 1.2/1.3 grid, blotted for 10 s at force 0 using a Mark IV Vitrobot and plunge-frozen in liquid ethane. Between four and ten grids were screened during each data collection, as ice thickness varied between grids. Optimization was performed on an in-house Polara electron microscope. Datasets were recorded on Titan Krios electron microscopes with K2 cameras at C-CINA (Basel) or at the ESRF (Grenoble). Details of data collections are shown in Extended Data Table 1.

Image processing. At the Basel Krios microscope, the data collection was monitored online and good images were selected using Focus[34]; images were acquired in super-resolution mode and binned by Fourier-space cropping during the drift correction. At the ESRF Krios microscope, the counted mode was used. Drift was corrected with MotionCor2[35] and dose-weighted sums were used for subsequent processing, except for CTF correction, which was performed using GCTF[36] on non-dose-weighted sums. Picking was performed with Gautomatch (http://www.mrc-lmb.cam.ac.uk/kzhang/Gautomatch/) using average from 2D classes as templates. Subsequent steps were performed using Relion[37] on a GPU workstation. Typically, two rounds of 2D classifications with 20–30 classes were performed, followed by a round of 3D classification without imposing symmetry (3–6 classes) with a low-pass-filtered initial model of the receptor. Particles presenting five-fold symmetry were selected, submitted to 3D classifications (classifications and data processing are further described in Extended Data Figs. 2, 4) and the best sets of particles were subjected to 3D auto-refinement. In the post-processing step, a soft mask was calculated and applied to the two half maps before the Fourier shell coefficient (FSC) was calculated. Map sharpening (B-factor fixed at −100 Å^2 for I1 and F, automatic estimation for T and I2) was also performed in the post-processing step. We tried the Phenix auto-sharpen program[38], which improved only the F map. The quality of the final reconstructions is shown in Extended Data Fig. 5.

Model refinement and structure analysis. Refinement was performed with the Phenix suite[39]. Cycles of real-space refinement were performed using global minimization, rigid body fit and local rotamer fitting (and B-factor refinement in late stages), alternating with manual rebuilding in Coot[40]. NCS and secondary structure restraints were enabled. The 4 models comprise residues 10–307 and 426–460. T, I1 and I2 also have MX and MA residues 308–330 and 399–426, which—owing to flexibility—could not be built in F. Tropisetron (numbered 902) was placed in the orthosteric site of T, and serotonin (numbered 901) was placed in the site of I1, F and I2. The densities for serotonin in I1 and F enable the ligand to be placed in several equivalent orientations, and we used the unambiguous density in I2 to choose the same ligand pose in these 3 structures. The stereochemical properties of the final models, analysed with the Molprobity server (http://molprobity.biochem.duke.edu/),

are reported in Extended Data Table 1. Pore profiles were plotted using HOLE[41], r.m.s.d. values were calculated with 'superpose' in the CCP4 suite[42]. Figures were prepared with the PyMOL Molecular Graphics System (Schrodinger), Chimera[43] or CueMol.

Molecular dynamics. Molecular assays were built for the four conformational states of 5-HT$_3$ described in the manuscript. For F, I1 and I2, we used the reported cryo-EM structures, whereas for the inhibited conformation we used the crystal structure (RCSB Protein Data Bank code (PDB): 4PIR) because of its higher resolution. The co-crystallized nanobodies were removed and the protein was modelled without serotonin. The five serotonins present in F, I1 and I2 structures were kept in the models. For I2, because no obvious densities were observed for TMPPAA, it was not represented in the model. The intracellular domain of the F conformation (not resolved in the cryo-EM density) was not included in the model.

Using the CHARMM-GUI web interface[44,45], each structure was embedded in a fully hydrated palmitoyl-oleyl-phosphatidylcholine (POPC) bilayer consisting of around 240 lipid units and about 30,000 for F and 42,000 water molecules for T, I1 and I2. K$^+$Cl$^-$ (150 mM) was explicitly added to each system, while ensuring their electric neutrality. The all-atom CHARMM36 force field[46] and revision thereof for lipids[47] were used to describe the system and CMAP corrections were introduced for the protein[48]. For water, we used the TIP3P model[49]. A subset of mass of the heavy atoms of lipids, protein and serotonin were transferred on the hydrogens atoms to which they are bound, to reach a hydrogen mass of 3.024 Da. Using such a mass repartitioning scheme, the equation of motions can be integrated with a time step of up to 4 fs without modifying the dynamics and thermodynamics of the system[50].

All simulations were carried out with the NAMD package v.2.12[51]. Simulations were performed in the isothermal–isobaric ensemble at $T = 300$K and $P = 1$ atm with anisotropic scaling of the simulation cell[52], long-range electrostatic interactions were treated with the particle-mesh Ewald method[53], and short-range electrostatics and Lennard-Jones interactions were smoothly truncated. The equations of motion were integrated with a time step of 4 and 8 fs for short- and long-range forces, respectively, using the Verlet r-RESPA multiple time-step propagator[54]. Covalent bonds involving hydrogen atoms were constrained to their equilibrium length by means of the 'rattle/shake algorithm'[55,56] and the 'settle' algorithm was used for water[57]. For each system, a smooth equilibration along which the positions of the heavy atoms of the protein were restrained harmonically, was carried out for 60 ns. After releasing the restraints, the simulations were extended up to 1 μs. All analyses and molecular rendering were achieved with VMD[58]. Pore radii were inferred using the program HOLE[41].

The potentials of mean force underlying the translocation of a potassium ion in the I1 and F conformations of the 5-HT$_3$ receptor were determined using a multiple-walker version[59] of the adaptive biasing force algorithm[60]. For the I1 conformation, the reaction coordinate model was chosen as the Euclidian distance between the ion and the centre of mass of the protein, projected onto its longitudinal axis; that is, the z-direction of Cartesian space. In the case of the F conformation, a two-dimensional free-energy landscape was generated, exploring ion diffusion in the pore not only longitudinally by means of the aforementioned projected Euclidian distance, but also radially. The potential of mean force along the pore was recovered by integration of the marginal law in the radial direction. The reaction pathway was broken down into 14 and 12 windows for the I1 and F conformations, respectively. The free-energy landscapes were explored by four walkers, syncing gradients every 500 molecular-dynamics steps. The total simulation time for the I1 and F conformations amounted to 2.16 and 3.04 μs, respectively, wherein the last 0.8 μs was used to estimate the error bars associated with the potentials of mean force, based on an independent mapping of the free-energy landscape by the walkers.

Electrophysiology. Electrical recordings were obtained by two-electrode voltage-clamp (TEVC) on *Xenopus* oocytes expressing either wild-type or mutated homomeric mouse 5-HT$_{3A}$ receptors. Mutants were obtained using the QuickChange Lightning (Stratagene) site-directed mutagenesis kit and oligonucleotides (Supplementary Table 2) to introduce point mutations into the pcDNA5/TO-m5-HT$_{3A}$ plasmid. All the mutations were verified by sequencing.

Oocytes were prepared as previously reported[61] using procedures that conformed to European regulations for animal handling and experiments, and were approved by governmental services (authorization no. D 38 185 10 001 for the animal facility delivered by the Prefect of Isère) and the Institutional Ethics Committee (ethics approval N° 12-040 granted to C. Moreau by the Ethics Committee of Commissariat à l'Energie Atomique et aux Energies Alternatives). Difolliculated oocytes were injected with 30 nl plasmid DNA (1–10 ng/μl) coding for the desired 5-HT$_{3A}$ subunit (subcloned into pcDNA5 vector). Microinjected oocytes were incubated for 1 to 5 days at 19 °C in Barth's solution (in mM: 1 KCl, 0.82 MgSO$_4$, 88 NaCl, 2.4 NaHCO$_3$, 0.41 CaCl$_2$, 16 HEPES, pH 7.4) supplemented with 100 U ml^{-1} penicillin and streptomycin.

Whole-cell TEVC recordings were obtained using an OC-725C Oocyte Clamp amplifier (Warner Instruments) at a constant holding potential of −50 mV.

Macroscopic currents were filtered at 1 kHz, digitized at 2 kHz with a Digidata 1440 analogue-to-digital interface and analysed with Clampfit (Molecular Devices). During the recordings, oocytes were constantly perfused with a 0 Ca-ND96 solution (containing in mM: 91 NaCl, 2 KCl, 1 $MgCl_2$, 5 HEPES, 1 EGTA, pH 7.4) at a rate of 1.3 ml/min, which allowed the application of serotonin and other compounds in a time range of seconds (20-fold concentration change of applied compounds in 5 s). Throughout this study, electrophysiological responses were induced by 10 μM serotonin (a saturating dose for all tested constructions, not shown) and peaked in less than 3 s. In all constructions tested, 10-min applications of serotonin induced almost complete desensitization (to less than 3% of the peak current with $t_{1/2}$ in the min range). Full recovery of desensitization was observed after washing serotonin for 10 min. Ca^{2+} ions are permeant through 5-HT$_3$ receptors[62]. Calcium was therefore carefully removed from the recording perfusion solution to avoid contamination of the serotonin-induced responses by endogenous oocyte current secondarily activated by Ca^{2+} ions entering the oocyte through the serotonin receptors.

MTSEA (2-aminoethyl methanethiosulfonate bromide) and MTSET (2-trimethylammonium-ethyl methanethiosulfonate bromide) were purchased from Interchim and prepared immediately before perfusion from stock solutions in water stored at −20 °C. The effect of MTS compounds on pore cysteine-mutants was studied using the following protocol: (i) checking stability of the response with a train of three to five applications of 10 μM serotonin for 10 s, every 5 min (I_{pre}); (ii) applying MTS compounds for 2 min at 1 mM, either in the absence of 5-HT (to probe cysteine accessibility in the resting state), simultaneously with 10 μM 5-HT (to probe the open state) or simultaneously with 10 μM 5-HT after a 10 min pre-application of 5-HT alone allowing for complete desensitization; (iii) following the effect of MTS compounds during a second set of five applications of 5-HT for 10 s every 5 min (I_{post}). Irreversible effects of MTS compounds were quantified by measuring I_{post} 25 min after removal of the MTS compound. The percentage of inhibition or potentiation was calculated as $(I_{pre}-I_{post})/I_{pre} \times 100$. MTS compounds (applied at 1 mM simultaneously with 10 μM serotonin) have no detectable effect on wild-type receptors (not shown).

Voltage-clamp fluorometry. VCF recordings were performed on *Xenopus* oocytes provided by Ecocyte Bioscience that were injected with 50 ng/μl plasmid DNA encoding for the mouse 5-HT$_{3A}$ receptor S19′C mutant, after 2 to 6 days of expression in Barth solution at 17 °C. They were labelled with MTS-TAMRA (Toronto Chemicals) for 5 min at 17 °C in ND96 buffer without $CaCl_2$ containing 10 μM 5-hydroxytryptamine (5-HT), then rinsed and stored at 17 °C for up to 4 h before recording in ND96. Recording were made in a TEVC setup as described[13], adapted for fluorescence recording. In brief, recordings were made with a VCF dedicated chamber with only a fraction of the oocyte perfused and illuminated by a LED (coolLED PE-4000). Light was collected using a fluorescence microscope (Zeiss Axiovert135) equipped with a 40× objective (Plan Neofluar), a TRITC filter set and a photomultiplier tube (Hamamatsu Photonics). Recordings were made at −60 mV clamp, 500-Hz sampling rate with a 550-nm excitation wavelength. Data were filtered, corrected for baseline and photobleaching where necessary, and analysed using pClamp and Axograph. Dose–response curves were fitted using Prism to the Hill equation: $I/I_{max} = 1/(1 + (EC_{50}/[5\text{-}HT])^{nH})$ in which I is the response at a given [5-HT] (serotonin concentration), I_{max} is the maximal response, EC_{50} is half maximal effective concentration and nH is the Hill coefficient. Serotonin dose–response relations were shifted to the left with half-responses for fluorescence and current at 40 and 240 nM, respectively (the EC_{50} of the wild-type receptor is 800 nM).

Fluorescence imaging plate reader membrane potential blue assay. The agonist properties of 5-HT and TMPPAA (Sigma-Aldrich) were characterized at human wild-type or mutant 5-HT$_{3A}$ receptors transiently expressed in tsA201 cells in the fluorescence imaging plate reader (FLIPR) membrane potential blue (FMP; fluoresence-based membrane potential) assay. The generation of some of the human 5-HT$_{3A}$ mutants have previously been described[63]. Other mutants were constructed by introduction of point mutations into the h5-HT3A-pCIneo plasmid using Quikchange II XL site-directed mutagenesis (Stratagene) and oligonucleotides (TAG Copenhagen). The absence of unwanted mutations in all cDNAs created by PCR was verified by sequencing (Eurofins MWG Operon). The cells were cultured in Dulbecco's Modified Eagle Medium supplemented with penicillin (100 U/ml), streptomycin (100 mg/ml) and 10% fetal bovine serum in a humidified atmosphere of 5% CO_2 and 95% air at 37 °C. Cells (1.2×10^6) were split into a 6-cm tissue culture plate, transfected the following day with 4 μg cDNA (wild-type or mutant h5-HT3A-pCIneo) using Polyfect (Qiagen) as transfection reagent, and split into poly-D-lysine-coated black 96-well plates (8×10^4 cells per well) with clear bottom (BD Biosciences) the following day. After 20–24 h following transfection, the medium was aspirated, and the cells were washed with 100 μl Krebs buffer (140 mM NaCl, 4.7 mM KCl, 2.5 mM $CaCl_2$, 1.2 mM $MgCl_2$, 11 mM HEPES, 10 mM D-glucose, pH 7.4). Then 100 μl Krebs buffer supplemented with 0.5 mg/ml FMP assay dye (Molecular Devices) was added to each well, and the 96-well plate was assayed at 37 °C in a FLEXStation3 Benchtop Multi-Mode Microplate Reader (Molecular Devices) measuring emission (in fluorescence units (FU)) at 565 nm caused by excitation at 530 nm before and up to 90 s after addition of 33.3 μl assay buffer supplemented with agonist (5-HT or TMPPAA). The experiments were performed in duplicate at least three times for each agonist at all receptors. Concentration–response curves for the agonists were constructed based on the difference in the fluorescence units (rFU) between the maximal fluorescence recording made before and after addition of the agonists at different concentrations. The curves were generated by non-weighted least-squares fits using the program KaleidaGraph (Synergy Software).

Reporting summary. Further information on research design is available in the Nature Research Reporting Summary linked to this paper.

Data availability

Atomic coordinates of the four conformations have been deposited in the Protein Data Bank with accession numbers 6HIN, 6HIO, 6HIQ and 6HIS for conformations F, I1, I2 and T, respectively. The cryo-EM density maps have been deposited in the Electron Microscopy Data Bank with accession numbers EMD-0225, EMD-0226, EMD-0227 and EMD-0228 for conformations F, I1, I2 and T, respectively.

30. Hassaïne, G. et al. Large scale expression and purification of the mouse 5-HT$_3$ receptor. *BBA Biomembranes* **1828**, 2544–2552 (2013).
31. Hassaïne, G. et al. Expression, biochemistry, and stabilization with camel antibodies of membrane proteins: case study of the mouse 5-HT$_3$ receptor. *Methods Mol. Biol.* **1635**, 139–168 (2017).
32. Yakel, J. L., Lagrutta, A., Adelman, J. P. & North, R. A. Single amino acid substitution affects desensitization of the 5-hydroxytryptamine type 3 receptor expressed in *Xenopus* oocytes. *Proc. Natl Acad. Sci. USA* **90**, 5030–5033 (1993).
33. Hu, X.-Q. & Lovinger, D. M. Role of aspartate 298 in mouse 5-HT$_{3A}$ receptor gating and modulation by extracellular Ca^{2+}. *J. Physiol. (Lond.)* **568**, 381–396 (2005).
34. Biyani, N. et al. Focus: The interface between data collection and data processing in cryo-EM. *J. Struct. Biol.* **198**, 124–133 (2017).
35. Zheng, S. Q. et al. MotionCor2: anisotropic correction of beam-induced motion for improved cryo-electron microscopy. *Nat. Methods* **14**, 331–332 (2017).
36. Zhang, K. Gctf: Real-time CTF determination and correction. *J. Struct. Biol.* **193**, 1–12 (2016).
37. Scheres, S. H. W. RELION: implementation of a Bayesian approach to cryo-EM structure determination. *J. Struct. Biol.* **180**, 519–530 (2012).
38. Terwilliger, T. C., Sobolev, O. V., Afonine, P. V. & Adams, P. D. Automated map sharpening by maximization of detail and connectivity. *Acta Crystallogr. D* **74**, 545–559 (2018).
39. Adams, P. D. et al. PHENIX: a comprehensive Python-based system for macromolecular structure solution. *Acta Crystallogr. D* **66**, 213–221 (2010).
40. Emsley, P., Lohkamp, B., Scott, W. G. & Cowtan, K. Features and development of Coot. *Acta Crystallogr. D* **66**, 486–501 (2010).
41. Smart, O. S., Neduvelil, J. G., Wang, X., Wallace, B. A. & Sansom, M. S. HOLE: a program for the analysis of the pore dimensions of ion channel structural models. *J. Mol. Graph.* **14**, 354–360 (1996).
42. Winn, M. D. et al. Overview of the CCP4 suite and current developments. *Acta Crystallogr. D* **67**, 235–242 (2011).
43. Pettersen, E. F. et al. UCSF Chimera—a visualization system for exploratory research and analysis. *J. Comput. Chem.* **25**, 1605–1612 (2004).
44. Jo, S., Kim, T., Iyer, V. G. & Im, W. CHARMM-GUI: a web-based graphical user interface for CHARMM. *J. Comput. Chem.* **29**, 1859–1865 (2008).
45. Wu, E. L. et al. CHARMM-GUI Membrane Builder toward realistic biological membrane simulations. *J. Comput. Chem.* **35**, 1997–2004 (2014).
46. MacKerell, A. D. et al. All-atom empirical potential for molecular modeling and dynamics studies of proteins. *J. Phys. Chem. B* **102**, 3586–3616 (1998).
47. Klauda, J. B. et al. Update of the CHARMM all-atom additive force field for lipids: validation on six lipid types. *J. Phys. Chem. B* **114**, 7830–7843 (2010).
48. Best, R. B. et al. Optimization of the additive CHARMM all-atom protein force field targeting improved sampling of the backbone φ, ψ and side-chain χ1 and χ2 dihedral angles. *J. Chem. Theory Comput.* **8**, 3257–3273 (2012).
49. Jorgensen, W. L., Chandrasekhar, J., Madura, J. D., Impey, R. W. & Klein, M. L. Comparison of simple potential functions for simulating liquid water. *J. Chem. Phys.* **79**, 926–935 (1983).
50. Hopkins, C. W., Le Grand, S., Walker, R. C. & Roitberg, A. E. Long-time-step molecular dynamics through hydrogen mass repartitioning. *J. Chem. Theory Comput.* **11**, 1864–1874 (2015).
51. Phillips, J. C. et al. Scalable molecular dynamics with NAMD. *J. Comput. Chem.* **26**, 1781–1802 (2005).
52. Feller, S. E., Zhang, Y., Pastor, R. W. & Brooks, B. R. Constant pressure molecular dynamics simulation: the Langevin piston method. *J. Chem. Phys.* **103**, 4613–4621 (1995).
53. Darden, T., York, D. & Pedersen, L. Particle mesh Ewald: an $N \cdot \log(N)$ method for Ewald sums in large systems. *J. Chem. Phys.* **98**, 10089–10092 (1993).
54. Tuckerman, M., Berne, B. J. & Martyna, G. J. Reversible multiple time scale molecular dynamics. *J. Chem. Phys.* **97**, 1990–2001 (1992).
55. Ryckaert, J.-P., Ciccotti, G. & Berendsen, H. J. C. Numerical integration of the cartesian equations of motion of a system with constraints: molecular dynamics of n-alkanes. *J. Comput. Phys.* **23**, 327–341 (1977).
56. Andersen, H. C. Rattle: A 'velocity' version of the shake algorithm for molecular dynamics calculations. *J. Comput. Phys.* **52**, 24–34 (1983).

57. Miyamoto, S. & Kollman, P. A. Settle: an analytical version of the SHAKE and RATTLE algorithm for rigid water models. *J. Comput. Chem.* **13**, 952–962 (1992).

58. Humphrey, W., Dalke, A. & Schulten, K. VMD: visual molecular dynamics. *J. Mol. Graph.* **14**, 33–38 (1996).

59. Comer, J., Phillips, J. C., Schulten, K. & Chipot, C. Multiple-replica strategies for free-energy calculations in NAMD: multiple-walker adaptive biasing force and walker selection rules. *J. Chem. Theory Comput.* **10**, 5276–5285 (2014).

60. Comer, J. et al. The adaptive biasing force method: everything you always wanted to know but were afraid to ask. *J. Phys. Chem. B* **119**, 1129–1151 (2015).

61. Moreau, C. J., Niescierowicz, K., Caro, L. N., Revilloud, J. & Vivaudou, M. Ion channel reporter for monitoring the activity of engineered GPCRs. *Methods Enzymol.* **556**, 425–454 (2015).

62. Yang, J. Ion permeation through 5-hydroxytryptamine-gated channels in neuroblastoma N18 cells. *J. Gen. Physiol.* **96**, 1177–1198 (1990).

63. Trattnig, S. M. et al. Discovery of a novel allosteric modulator of 5-HT$_3$ receptors: inhibition and potentiation of Cys-loop receptor signaling through a conserved transmembrane intersubunit site. *J. Biol. Chem.* **287**, 25241–25254 (2012).

64. Suryanarayanan, A. et al. The loop C region of the murine 5-HT$_{3A}$ receptor contributes to the differential actions of 5-hydroxytryptamine and *m*-chlorophenylbiguanide. *Biochemistry* **44**, 9140–9149 (2005).

65. Yan, D., Schulte, M. K., Bloom, K. E. & White, M. M. Structural features of the ligand-binding domain of the serotonin 5HT$_3$ receptor. *J. Biol. Chem.* **274**, 5537–5541 (1999).

66. Ruepp, M.-D., Wei, H., Leuenberger, M., Lochner, M. & Thompson, A. J. The binding orientations of structurally-related ligands can differ; a cautionary note. *Neuropharmacology* **119**, 48–61 (2017).

67. Kesters, D. et al. Structural basis of ligand recognition in 5-HT$_3$ receptors. *EMBO Rep.* **14**, 49–56 (2013).

68. Hibbs, R. E. et al. Structural determinants for interaction of partial agonists with acetylcholine binding protein and neuronal α7 nicotinic acetylcholine receptor. *EMBO J.* **28**, 3040–3051 (2009).

69. Spurny, R. et al. Pentameric ligand-gated ion channel ELIC is activated by GABA and modulated by benzodiazepines. *Proc. Natl Acad. Sci. USA* **109**, E3028–E3034 (2012).

70. Delbart, F. et al. An allosteric binding site of the α7 nicotinic acetylcholine receptor revealed in a humanized acetylcholine-binding protein. *J. Biol. Chem.* **293**, 2534–2545 (2018).

71. Steward, L. J. et al. Importance of phenylalanine 107 in Agonist recognition by the 5-hydroxytryptamine$_{3A}$ receptor. *Mol. Pharmacol.* **57**, 1249–1255 (2000).

72. Purohit, P. & Auerbach, A. Acetylcholine receptor gating at extracellular transmembrane domain interface: the 'pre-M1' linker. *J. Gen. Physiol.* **130**, 559–568 (2007).

73. Lee, W. Y. & Sine, S. M. Principal pathway coupling agonist binding to channel gating in nicotinic receptors. *Nature* **438**, 243–247 (2005).

74. Hu, X.-Q., Zhang, L., Stewart, R. R. & Weight, F. F. Arginine 222 in the pre-transmembrane domain 1 of 5-HT$_{3A}$ receptors links agonist binding to channel gating. *J. Biol. Chem.* **278**, 46583–46589 (2003).
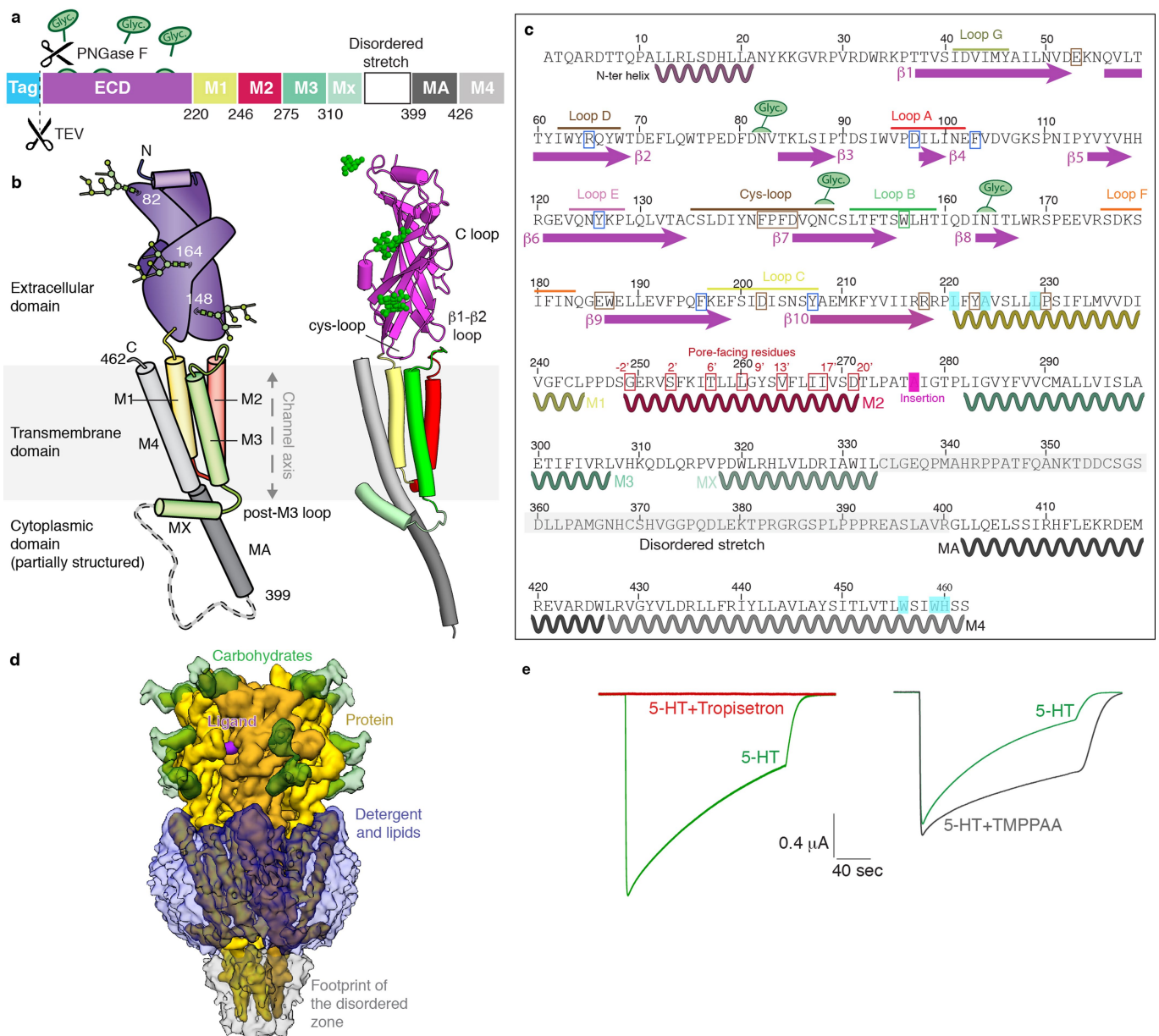
Extended Data Fig. 1 | 5-HT₃ receptor topology and sequence.
a, Schematic of the full-length 5-HT₃ receptor. The colour code is the same for all panels. Scissors indicate the enzymatic treatments used during purification: purification tag removal using TEV protease, and partial removal of carbohydrates using PNGase F. **b**, Topology scheme and structure of one subunit of the 5-HT₃ receptor. **c**, Sequence and numbering of the mouse 5-HT₃A receptor used in the present study. Secondary structures and important loops are indicated. Neurotransmitter site binding loops are highlighted. Important residues discussed in the study are boxed (pore-facing in red, sandwich motif in brown and neurotransmitter site in blue). Cyan highlights residues important for TMPPAA potency. Glycosylation sites are depicted in green. The mouse receptor used for this study is a variant compared to the consensus

sequence as it contains an alanine insertion in the M2–M3 loop, which is highlighted by the pink box. Notably, this insertion is present in the consensus human receptor sequence. This panel is adapted from ref. [5].
d, A typical unmasked reconstruction, with different density levels overlaid depicting the protein itself (yellow), ligands (purple), linked glycans (green), the detergent-lipid belt (transparent purple) and the footprint of the disordered zone (transparent grey). **e**, Currents induced in *Xenopus* oocytes expressing the mouse 5-HT₃A receptor by a 3-min application of 10 μM serotonin (green traces), co-application of 10 μM serotonin and 100 nM tropisetron (following a 5-min pre-application of tropisetron, red trace), co-application of 10 μM serotonin and 10 μM of TMPPAA (following a 5-min pre-application of TMPPAA, black trace). Current traces are representative of 3 independently repeated experiments.
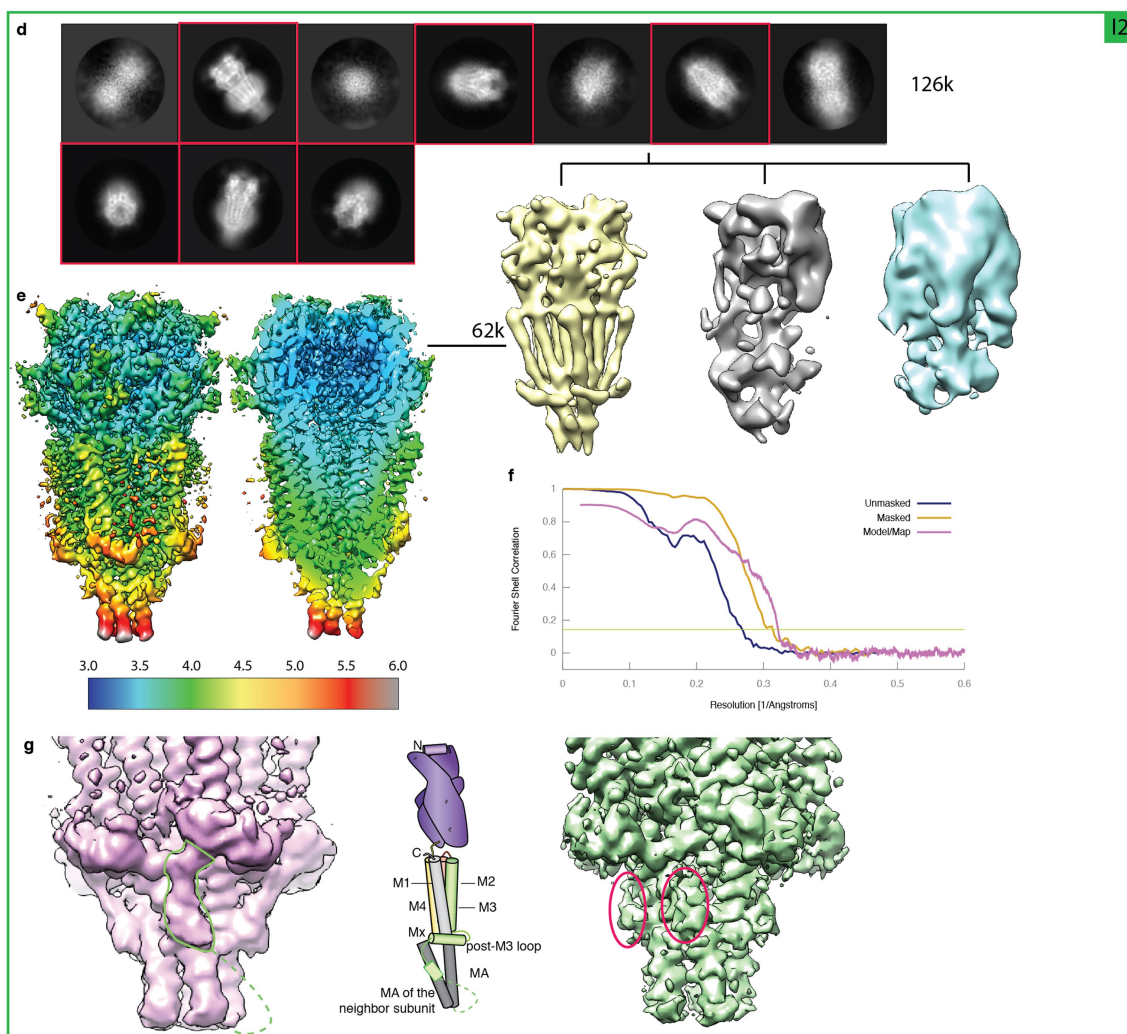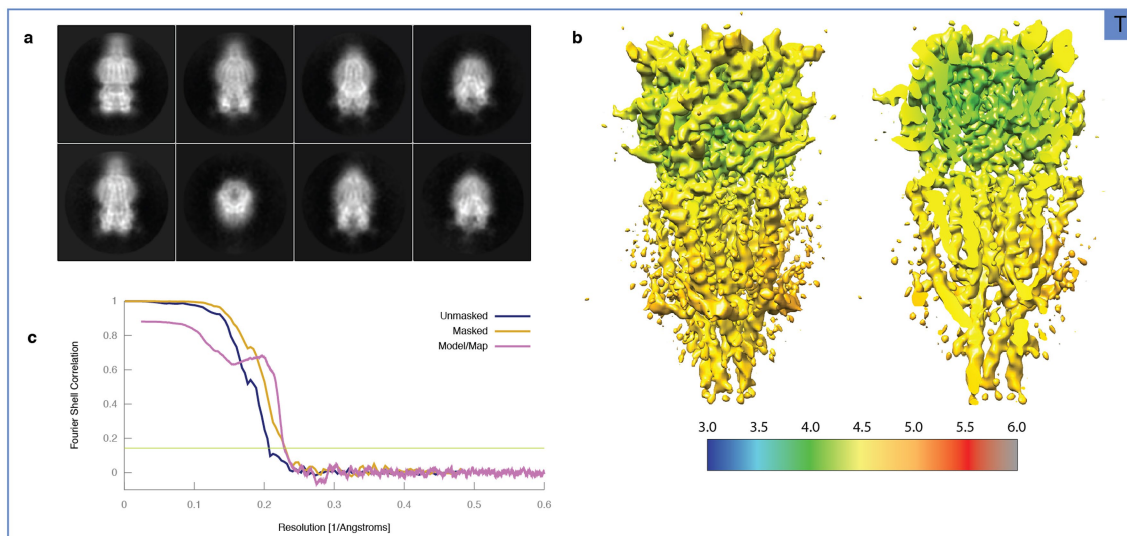
Extended Data Fig. 2 | See next page for caption.

Extended Data Fig. 2 | Electron microscopy and 3D reconstructions for the tropisetron dataset (T), and for the serotonin + TMPPAA dataset (I2). **a**, Tropisetron dataset (T). Selection of 2D class averages from the set of particles used for refinement of the tropisetron reconstruction. **b**, Three-dimensional reconstruction from the tropisetron dataset, filtered and coloured according to RELION local resolution. A global and a cut-through side view are shown. **c**, FSC curves for the density map before and after RELION post-processing, and between the model and the final map. **d**, Serotonin + TMPPAA dataset (I2). Selection of good 2D classes after one round of classification yields a set of 126,000 particles. One round of 3D classification with no symmetry imposed yields one class with pentameric symmetry, amounting to 62,000 particles. **e**, Unmasked unsharpened refined 3D reconstruction, filtered and coloured according to RELION local resolution. The colour range for resolution is similar to the equivalent representations for the other datasets in Extended Data

Fig. 4c, allowing direct comparison. **f**, FSC curves for the density map before and after RELION post-processing, and between the model and the final map. **g**, Left, a non-sharpened map filtered at 3.9 Å resolution, obtained with a subset of 55,000 particles from the I2 dataset, selected after further 3D classification focused on the ICD. The hypothetical trajectory of the polypeptide chain after MX is bordered by a green line. No full connectivity can be visualized and the model was not built. The chain appears to descend abruptly after MX, and may interact with MA of the neighbouring subunit at the level of H411, where there is a clear density. Then it must link to the beginning of MA, but maps show no information how it may do so. The schematic representation highlights that this putative trajectory contacts MA on the neighbouring subunit close to residue H411. Right, the corresponding sharpened and masked reconstruction, showing that model building is not possible. The density of the disordered stretch closed to H411 is highlighted by the pink ellipses.
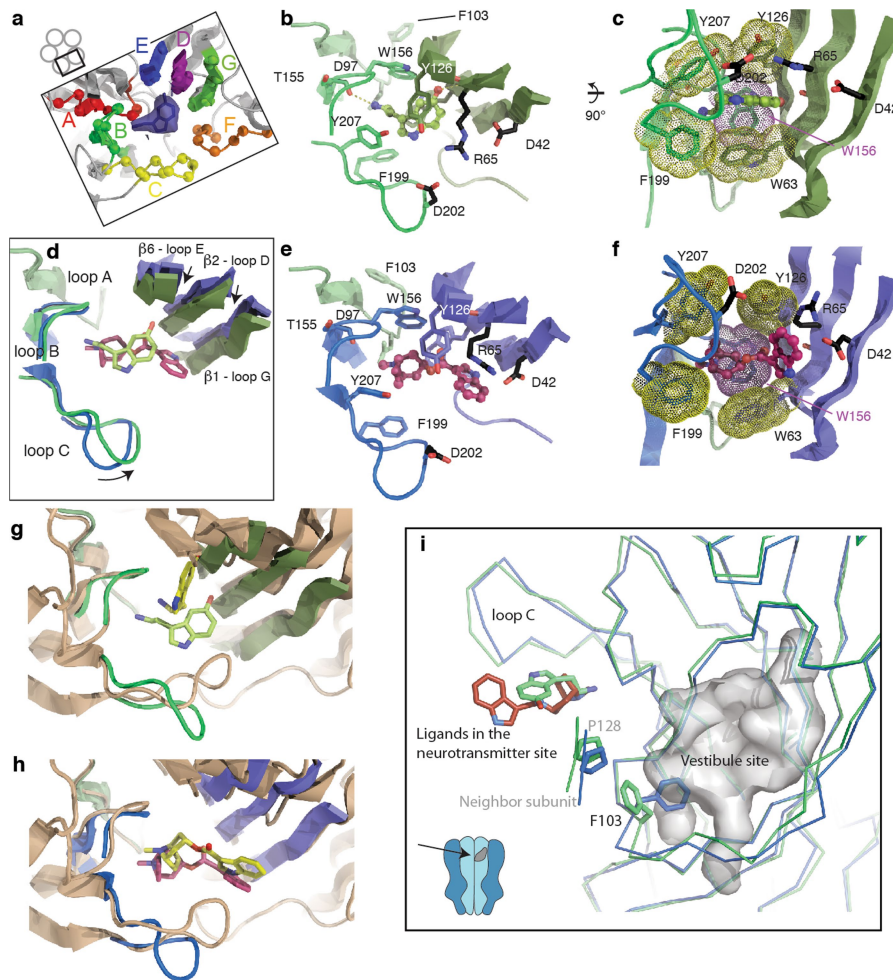
Extended Data Fig. 3 | Serotonin and tropisetron bound in the orthosteric site; the vestibule allosteric site. a, Organization of one of the five equivalent binding sites at the subunit interfaces in the ECD. Binding loops A–C are located on the principal subunit, and binding elements D–G are on the complementary subunit. The density around serotonin in the I2 reconstruction is shown as a transparent blue surface. **b**, **c**, Serotonin (ball-and-stick) in the orthosteric site in the I2 structure. Aromatic residues (dotted surfaces in **c**), hydrogen bonds with main chain atoms (dashed lines) and charged residues within salt-bridge distances (D202 on the principal side, R65 on the complementary side) are noted in two orthogonal views. Of note, mutants D202A[64] and R65A[65] exhibit impaired serotonin binding with increases of around 140-fold and 50-fold, respectively, in K_i (the equilibrium inhibitor constant) during competition assay for [³H]-granisetron binding. **d**, Superimposition of tropisetron-bound T (blue) and serotonin-bound I2 (green) structures, highlighting loop C motion and quaternary reorganization with arrows (principal subunit superposition in this panel and in **g** and **h**; note complementary subunit β-strand shift). Serotonin (light green) and tropisetron (magenta) are represented as sticks. **e**, **f**, Tropisetron bound to the orthosteric site in the T structure. The bicyclic tropane moiety is sandwiched between W156 of loop B and Y207 of loop C, whereas the indole lies close to R65, W63 in loop D, D42 and I44 in loop G, and R169 in loop F. Functional exploration of the binding mode of tropisetron consistently showed that, among others, single mutations to cysteine of the aromatic residues W156, Y207 or W63 abolished binding[66]. To fit tropisetron, the side chain of R65

is pushed upward and in turn displaces the side chains of Y67 and W168, compared to the empty orthosteric site of the X-ray structure. Densities for these side chains are not well-resolved. The density for tropisetron is shown in Extended Data Fig. 5f. **g**, Superposition of the I2 structure with the crystal structure of a mutant acetylcholine binding protein (AChBP, wheat cartoon) in complex with serotonin[67] (yellow sticks) shows distinct binding modes. **h**, Superposition of the T structure with the crystal structure of AChBP (wheat cartoon) in complex with tropisetron (yellow sticks) shows similar interactions with the protein at loop C, D, E, F and G (not shown for clarity), consistent with the 3 orders of magnitude difference (0.7 versus 479 nM[68]) in K_d (dissociation constant). **i**, Overlay of the T and I2 structures (in blue and green, respectively) superimposed on a subunit ECD, showing the motion of F103 out of the vestibule site. The protein depicted as ribbon is viewed from inside the vestibule, and the intra-subunit cavity (in the I2 conformation) is represented as a grey surface. Acetate in GLIC, flurazepam in the bacterial homologue ELIC[69] or a drug fragment in α7-AChBP[70] bind to this cavity. A putative rationale for the strong effect of F103 mutants on serotonin EC_{50}[71], despite its absence of participation in the binding site, comes from the observation of its concerted motion with that of strands from the neighbouring subunit (around P128 and around P110; for clarity, the latter is not represented here). Therefore, the motion of F103 may participate in subunit–subunit quaternary reorganization, exemplifying the allosteric coupling between sites.
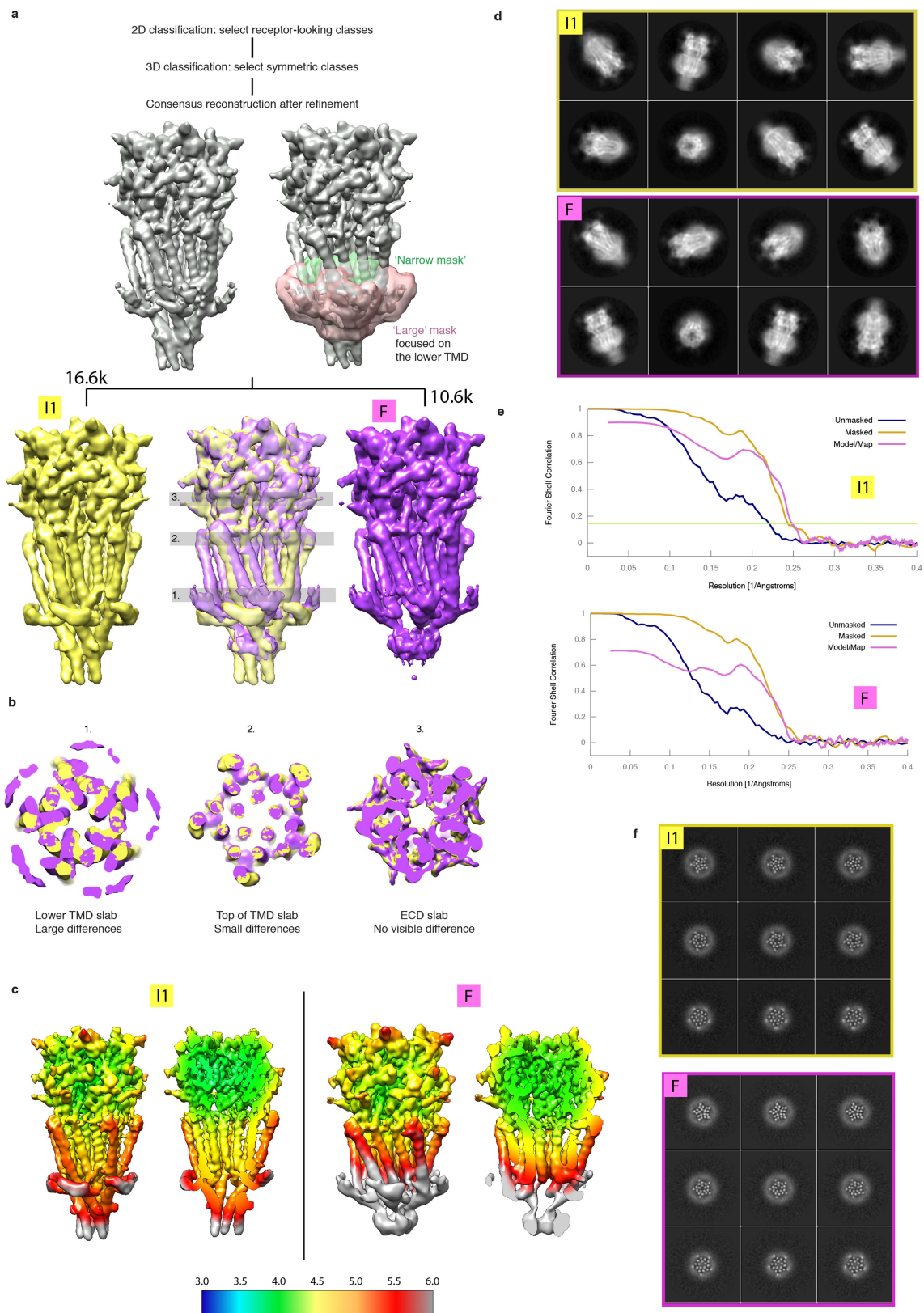
Extended Data Fig. 4 | See next page for caption.

Extended Data Fig. 4 | Electron microscopy, classifications and 3D reconstructions for the serotonin dataset. a, Schematic of the data processing, with classical rounds of 2D and 3D classification yielding a consensus reconstruction seen parallel to the membrane plane (grey) where helices look like tubes of elliptic sections, indicating heterogeneity. Extensive classification trials, without alignment, with masks of various size covering the lower part of the TMD (shown in green and red) enable two conformations to be distinguished (yellow corresponding to the I1 structure, and purple corresponding to the F structure), representing the extreme positions of the helices in the consensus reconstruction. An overlay of the two reconstructions depicts the good superimposition of the ECD and the clear difference in the lower TMD. Grey rectangles indicate the positions of the slabs represented in **b**. All reconstructions shown are unmasked outputs of RELION 3D refinements. **b**, Slabs, viewed perpendicular to the membrane plane, from the intracellular side showing the overlay of the I1 and the F reconstructions. **c**, Reconstructions filtered and coloured according to RELION local resolution. A global and a cut-through side view are shown. **d**, Selection of 2D class averages from the set of particles used for refinement of the I1 and F reconstructions. **e**, FSC curves showing the unmasked and masked FSCs (before and after post-processing in RELION), and the model-to-map FSC. **f**, Selection of 'slice' views of the TMD of the final unmasked unsharpened reconstructions.
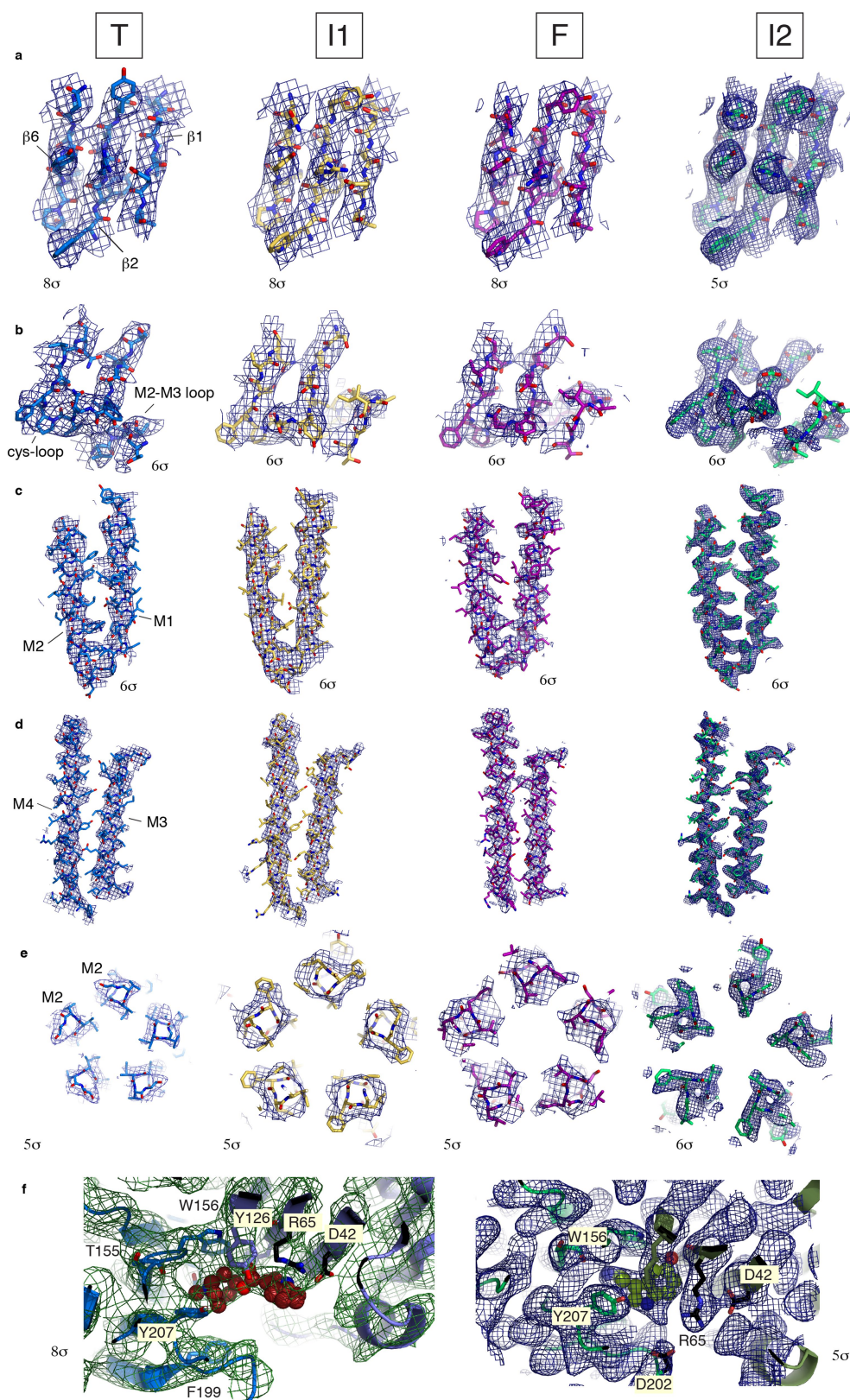
Extended Data Fig. 5 | Quality of the density maps in representative regions of the four 5-HT₃ receptor reconstructions. Densities in mesh representations overlaid with structures for the T (blue), I1 (yellow), F (purple) and I2 (green) reconstructions and structures, left to right, respectively, in each panel. Views **a**–**e** are approximately the same as those in extended data figure 4 of a previous publication of α1 GlyR[7]. **a**, Representative densities of the β-sheets in the ECD. **b**, Densities of the Cys loop and the M2–M3 loop. **c**, Densities of helices M1 and M2.

d, Densities of M3 and M4. **e**, Densities of M2 at the level of L9′ (L260). **f**, Densities around the ligands tropisetron (in T) and serotonin (in I2). The 3.2 Å resolution of I2 permits unambiguous orientation of serotonin, and side chains of residues around the ligands are seen in densities. For tropisetron, given the limited 4.5 Å global resolution, the orientation of the ligand and the positions of surrounding side chain are less certain. The views are the same as in Extended Data Fig. 3b, e.
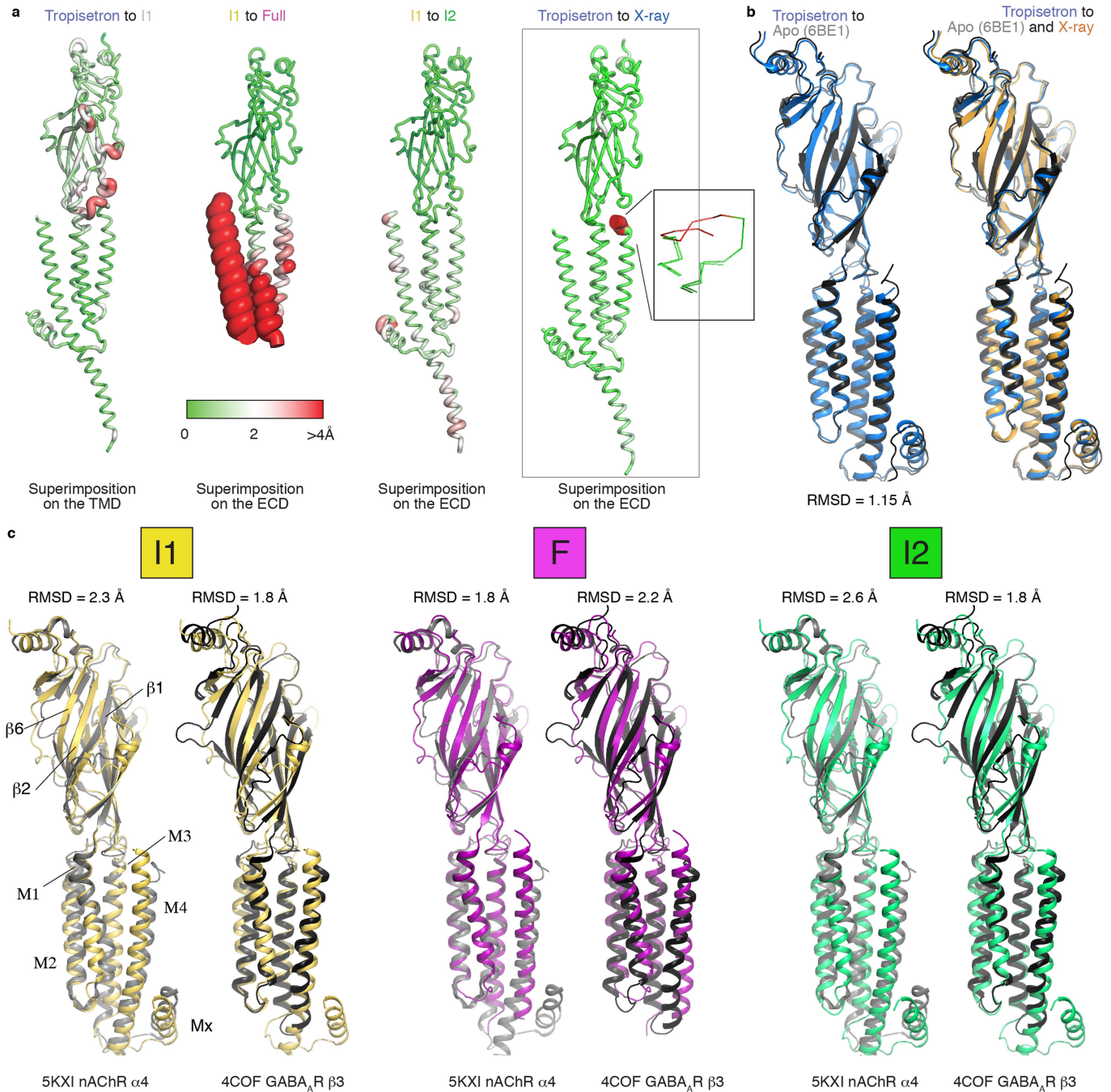
Extended Data Fig. 6 | Structural superpositions with the nAChR α4β2, the GABA_A receptor β3 subunit and the apo 5-HT_3 receptor structures. **a**, Putty representations of pairwise deviations for the 5-HT_3 receptor conformations. The selection used for superimposition, and the two conformations used, are noted for each image. The colour code and tube thickness code are the same for all images. In the T versus X-ray image, the red zone corresponds to a loop that was not modelled in the X-ray structure. **b**, Superimposition of a 5-HT_3 receptor subunit in the inhibited T state (blue) and of a 5-HT_3 receptor subunit in the apo state (grey, PDB: 6BE1). Structures are globally similar with differences in the lipid-exposed helices M3, MX and M4, hypothetically a consequence of the different additives used—a lipid mixture in this study versus fluorinated fos-choline 8 for the apo structure. Superposition of the T structure (blue), the apo structure (grey) and the X-ray structure (orange). **c**, Superposition of a 5-HT_3 receptor subunit in the I1, I2 and F conformations with a nAChR α4 subunit (PDB: 5KXI, chain A) or a GABA_A receptor β3 subunit (PDB: 4COF). C_α r.m.s.d. is noted. Comparison of superpositions with r.m.s.d. below 2 Å shows that in the case of F and nAChR α4 (middle, purple and grey), the domain-to-domain orientation is very similar and the extracellular halves of helices M1, M2, M3 superimpose very well, whereas clear deviations are present in their intracellular halves and at the level of M4 (r.m.s.d. without M4 drops to 1.6 Å). In the case of I1 and GABA_A β3 (left, yellow and black), or I2 and GABA_A β3 (right, green and black), differences are more distributed; deviations of the ECD indicate different domain-to-domain orientations, and in the TMD M1 and M3 superimpose quite well but M2 and M4 clearly differ.
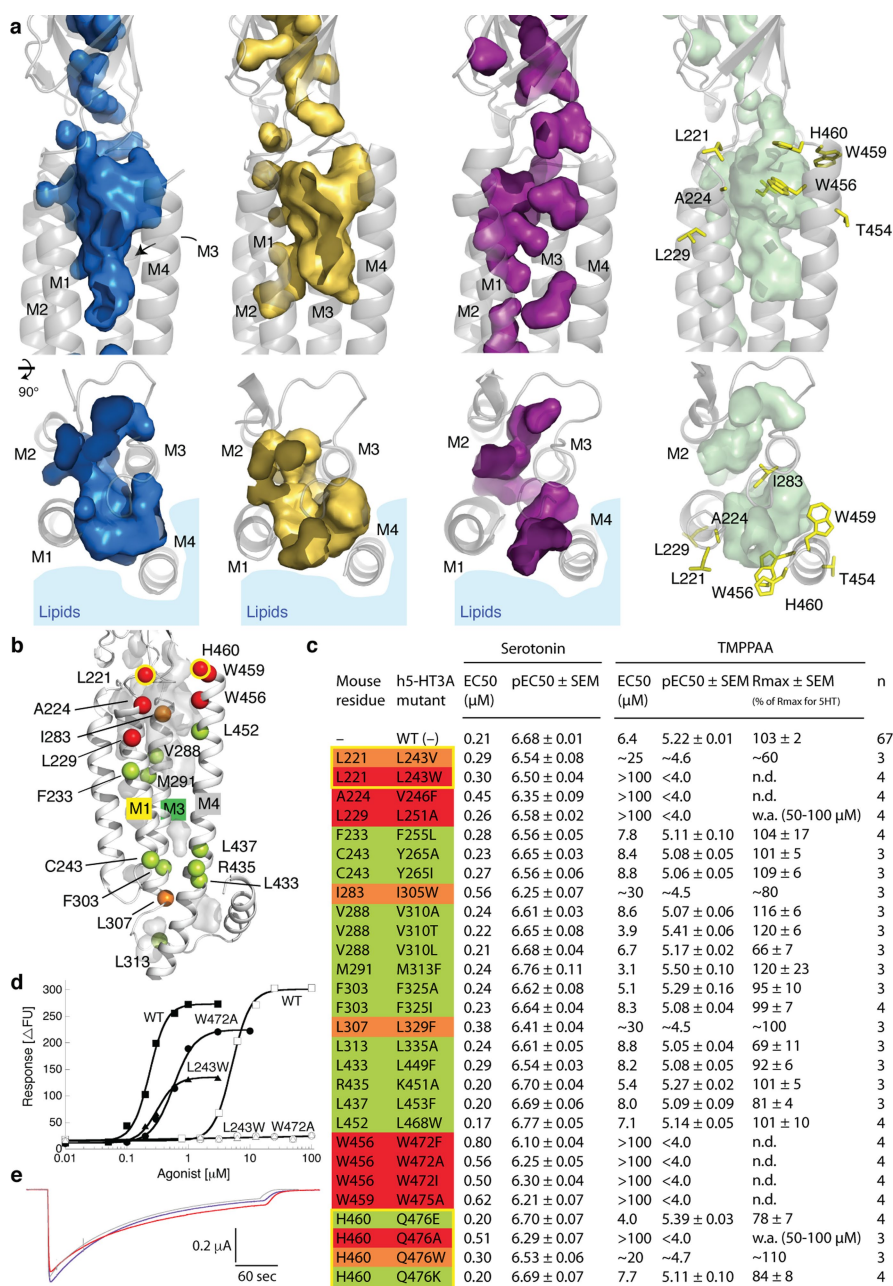
Extended Data Fig. 7 | TMPPAA binds to an allosteric site in the TMD.

a, Cavities in surface mode for the T (blue), I1 (yellow), F (purple) and I2 (green) states. Note the re-arrangement of the cavities between states. The protein is depicted in cartoon, with sticks in the right panels for residues in which mutations impair the effect of TMPPAA. Noisy densities are found in the I2 reconstruction, in or close to the cavities, but they do not permit ligand modelling and could correspond to parts of a lipid or detergent molecule. **b**, Side view of the trans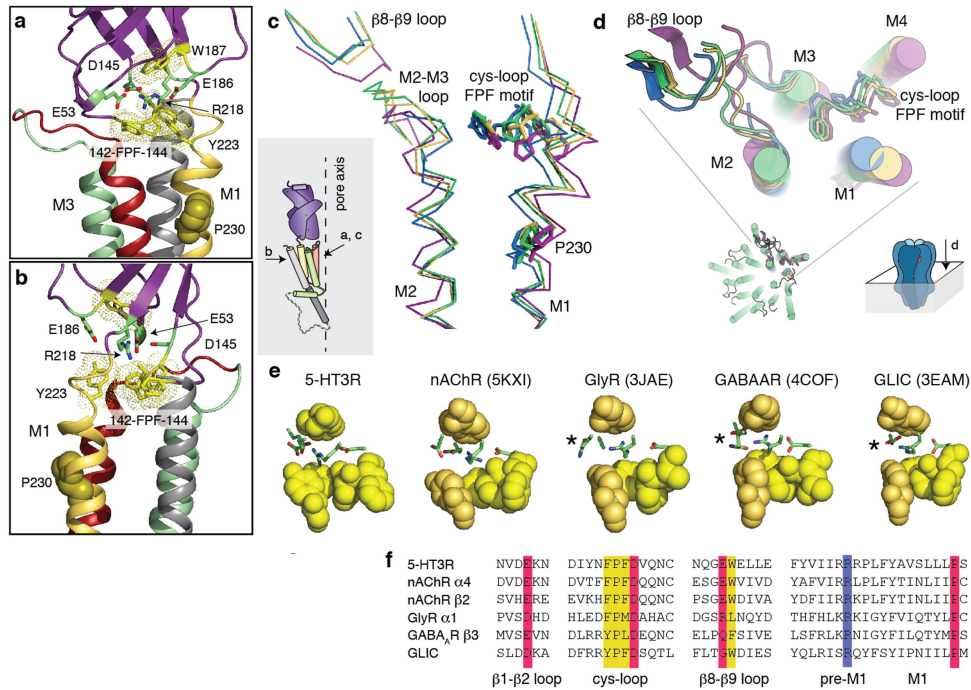membrane domain of I2 with mutated positions depicted as green spheres (for residues for which mutations had negligible effect on TMPPAA potency), orange spheres (for residues for which mutations reduced TMPPAA potency substantially) or red spheres (for mutations that completely or almost completely eliminated TMPPAA activity at concentrations up to 100 μM). Yellow circles indicate residues for which different mutations produced different effects. **c**, Functional properties exhibited by serotonin and TMPPAA as agonists at 5-HT$_{3A}$ receptors expressed in tsA201 cells in an FMP assay. The human 5-HT$_{3A}$ receptor was used for these experiments, since TMPPAA evokes a more robust agonist response through this receptor than through mouse

5-HT$_{3A}$ in this assay[17]. The colour code is similar to that in **b**. n.d., not determinable, w.a., weak activity. A complete table of data for all tested mutant receptors is shown in Supplementary Table 1. **d**, Concentration-response curves for serotonin (closed symbols) and TMPPAA (open symbols) tested as agonists at wild-type, W472A and L243W human 5-HT$_{3A}$ receptors expressed in tsA201 cells, using the FMP assay. Data are from a single representative experiment determined in the same 96-well plate and are given as mean based on duplicate determinations. The experiment was repeated independently with similar results 3 times for the W472A and L243W receptors and 66 times for the wild-type receptor (*n* for wild-type and all mutant receptors are given in **c**). **e**, Loss of TMPPAA potency at the mouse W456A mutant receptor. Currents evoked by 10 μM serotonin (blue curve) or 10 μM serotonin plus 100 μM TMPPAA (red curve) are equivalent. The grey trace, obtained in an oocyte expressing wild-type receptors (response to 10 μM serotonin, normalized for the peak amplitude), shows that desensitization in wild-type and W456A mutant receptors is similar. Current traces are representative of 3 independently repeated experiments.

c

Mouse residue	h5-HT3A mutant	Serotonin EC50 (μM)	Serotonin pEC50 ± SEM	TMPPAA EC50 (μM)	TMPPAA pEC50 ± SEM	TMPPAA Rmax ± SEM (% of Rmax for 5HT)	n
–	WT (–)	0.21	6.68 ± 0.01	6.4	5.22 ± 0.01	103 ± 2	67
L221	L243V	0.29	6.54 ± 0.08	~25	~4.6	~60	3
L221	L243W	0.30	6.50 ± 0.04	>100	<4.0	n.d.	4
A224	V246F	0.45	6.35 ± 0.09	>100	<4.0	n.d.	4
L229	L251A	0.26	6.58 ± 0.02	>100	<4.0	w.a. (50-100 μM)	4
F233	F255L	0.28	6.56 ± 0.05	7.8	5.11 ± 0.10	104 ± 17	4
C243	Y265A	0.23	6.65 ± 0.03	8.4	5.08 ± 0.05	101 ± 5	3
C243	Y265I	0.27	6.56 ± 0.06	8.8	5.06 ± 0.05	109 ± 6	3
I283	I305W	0.56	6.25 ± 0.07	~30	~4.5	~80	3
V288	V310A	0.24	6.61 ± 0.03	8.6	5.07 ± 0.06	116 ± 6	3
V288	V310T	0.22	6.65 ± 0.08	3.9	5.41 ± 0.06	120 ± 6	3
V288	V310L	0.21	6.68 ± 0.04	6.7	5.17 ± 0.02	66 ± 7	3
M291	M313F	0.24	6.76 ± 0.11	3.1	5.50 ± 0.10	120 ± 23	3
F303	F325A	0.24	6.62 ± 0.08	5.1	5.29 ± 0.16	95 ± 10	3
F303	F325I	0.23	6.64 ± 0.04	8.3	5.08 ± 0.04	99 ± 7	4
L307	L329F	0.38	6.41 ± 0.04	~30	~4.5	~100	3
L313	L335A	0.24	6.61 ± 0.05	8.8	5.05 ± 0.04	69 ± 11	3
L433	L449F	0.29	6.54 ± 0.03	8.2	5.08 ± 0.05	92 ± 6	3
R435	K451A	0.20	6.70 ± 0.04	5.4	5.27 ± 0.02	101 ± 5	3
L437	L453F	0.20	6.69 ± 0.06	8.0	5.09 ± 0.09	81 ± 4	3
L452	L468W	0.17	6.77 ± 0.05	7.1	5.14 ± 0.05	101 ± 10	4
W456	W472F	0.80	6.10 ± 0.04	>100	<4.0	n.d.	4
W456	W472A	0.56	6.25 ± 0.05	>100	<4.0	n.d.	4
W456	W472I	0.50	6.30 ± 0.04	>100	<4.0	n.d.	4
W459	W475A	0.62	6.21 ± 0.07	>100	<4.0	n.d.	4
H460	Q476E	0.20	6.70 ± 0.07	4.0	5.39 ± 0.03	78 ± 7	4
H460	Q476A	0.51	6.29 ± 0.07	>100	<4.0	w.a. (50-100 μM)	3
H460	Q476W	0.30	6.53 ± 0.06	~20	~4.7	~110	3
H460	Q476K	0.20	6.69 ± 0.07	7.7	5.11 ± 0.10	84 ± 8	4

Extended Data Fig. 8 | Structural motif and reorganization at the ECD–TMD interface. a, b, Key interacting charged residues R218 (pre-M1, key in gating[72–74]), E53 (loop β1–β2), E186 (loop β8–β9, conserved only in cationic eukaryotic receptors) and D145 (Cys loop)—represented as purple sticks—are sandwiched between conserved essential aromatic residues (FPF motif of the Cys loop, W187 of β8–β9 and Y223 of M1), represented as yellow sticks and dots. Lower in the membrane, the strictly conserved P230—represented as spheres—enables M1 to kink. This structural organization is common to all pLGICs of known structure. Orientations of the views are indicated on the topology scheme. **c, d**, Side and top views depicting the concerted relative positions of the Cys-loop FPF 'wedge', represented as sticks, of transmembrane helices and of the β8–β9 loop. Compared to the inhibited structure, the wedge moves towards and pushes on M1 and also moves towards M4 in I1, I2 and F. F presents the biggest re-organization in this zone: M1, the M2–M3 loop and M3 follow the motion of the FPF motif, and M2 moves away from the pore axis (that is, to the back in the view in **c** and to the top in **d**). **e**, Conservation of the 'sandwich' structural motif in representative pLGIC structures. The aromatic top and bottom layers are represented as spheres (yellow, Cys loop; orange, β8–β9 loop and pre-M1 residue) whereas the central layer of charges is depicted as sticks. Note that in anionic receptors and GLIC, the charge of β8–β9 is absent (noted with a star). **f**, Sequence alignment of the motif residues in representative pLGIC structures.
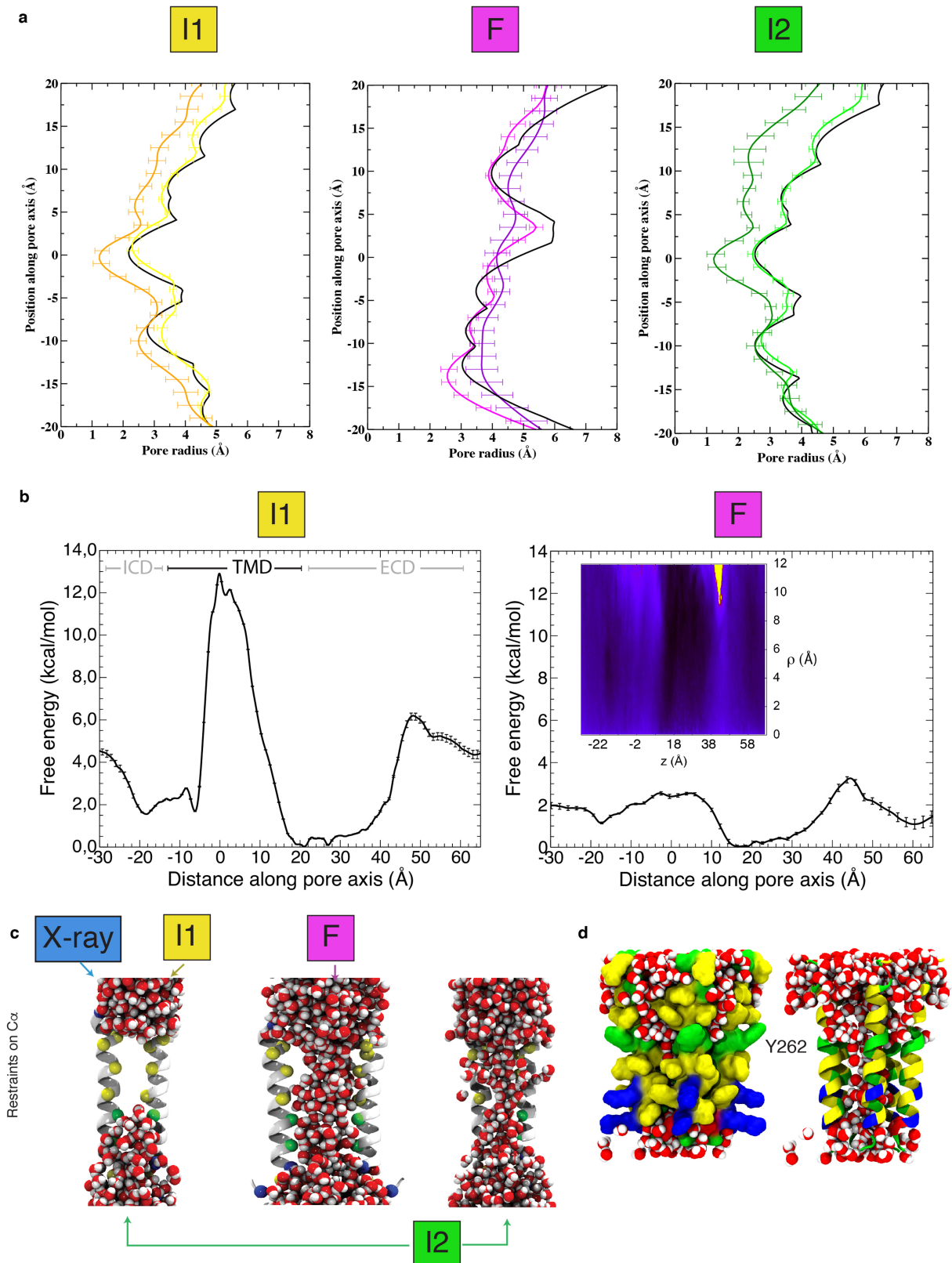
Extended Data Fig. 9 | See next page for caption.

Extended Data Fig. 9 | Geometry of the pore during the molecular dynamics simulations. a, HOLE transmembrane pore profiles for the trajectories starting from I1, F and I2. In each graph, the profile from the cryo-EM structure is represented in black, the average profile during the restrained part of the simulation (30–60 ns, mean ± s.d. of $n = 30$ snapshots taken every ns) in the lighter colour and the average profile during the unrestrained part (60–1,000 ns, mean ± s.d. of $n = 940$ snapshots taken every ns) in the darker colour. The y-axis origin corresponds to L260/9′ whereas S253/2′s is located at about −12 Å. **b**, Complete potentials of mean force of K^+ ions as a function of position along the pore axis. The inset represents the 2D free-energy landscape as a function of the position along the pore axis and the radial direction, orthogonal to it. The represented free-energy profile is the mean of 135,000,000 values distributed along 2.16 μs of the I1 trajectory (190,000,000 values distributed along 3.04 μs of the F trajectory); the standard deviation corresponds in both cases to 50,000,000 values from four independent walkers, distributed along the last 0.8 μs of the trajectory. **c**, Representative snapshots of the pore wetting during the initial restrained part (30–60 ns) of the simulations. A dewetted pore is observed for the T and I1 trajectories, a fully wetted one for the F trajectory, whereas wetting and dewetting occur in the I2 trajectory. C_α atoms of pore-exposed residues are represented as spheres. **d**, Snapshot of the I2 trajectory showing the wetting of grooves at the back of M2 (shown as molecular surface on the left, as cartoon on the right), concomitant with wetting of the pore.
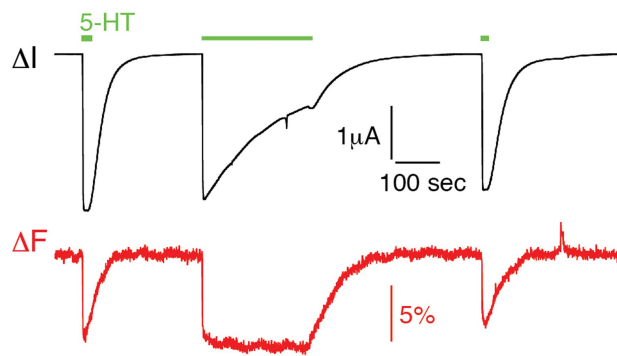
Extended Data Fig. 10 | Local motions in the pore probed by VCF.
Representative serotonin-evoked simultaneous current and fluorescence
recordings from oocytes expressing S19′C mutant receptors labelled
with MTS-TAMRA. Similar traces were obtained in 3 independent
experiments.

Extended Data Table 1 | Statistics of 3D reconstructions and model refinement

	Tropisetron	Serotonin		Serotonin and TMPPAA
Data collection and processing				
Microscope	Krios@CCINA	Krios@CCINA		Krios@ESRF
Magnification	130,000	130,000		130,000
Voltage (kV)	300	300		300
Electron exposure (e-/Å^2)	~80	~60		~50
Defocus range (µm)	0.5-2.5	0.8-2.5		0.8-2.5
Pixel size (Å)	0.52	0.52		1.067
Symmetry imposed	C5	C5		C5
Number of images	~1500	~2000		~3000
Particles picked	160k	456k		250k
Symmetric-looking particles	133k	145k		62k
Particles refined	43,558	16,660	10,667	62,032
Refinement	**T**	**I1**	**F**	**I2**
Initial model used	4PIR	4PIR	4PIR	4PIR
Resolution (Å)	4.5	4.2	4.1	3.2
FSC threshold	0.143	0.143	0.143	0.143
Map sharpening B-factor (Å^2)	-247	-100	-100	-127
Model composition				
Non-hydrogen protein atoms	15,645	15,670	13,805	15,670
Protein residues	1,935	1,925	1,675	1,925
Ligands	585	415	415	415
B-factor (Å^2)				
protein	127	130	83	78
ligand	113	102	73	53
R.M.S deviations				
Bond lengths (Å)	0.008	0.009	0.009	0.006
Bond angles (°)	1.5	1.1	1.2	1.0
Validation				
Molprobity score	2.0	1.45	1.35	1.18
Clashscore	14.1	8.3	6.4	3.9
Poor rotamers (%)	0.3	0.2	0.3	0.3
Ramachandran plot				
Favored (%)	95.1	98.0	98.5	98.4
Allowed (%)	4.9	2.0	1.5	1.6
Disallowed (%)	0.0	0.0	0.0	0.0

nature research

Corresponding author(s): NURY Hugues

Reporting Summary

Nature Research wishes to improve the reproducibility of the work that we publish. This form provides structure for consistency and transparency in reporting. For further information on Nature Research policies, see Authors & Referees and the Editorial Policy Checklist.

Statistical parameters

When statistical analyses are reported, confirm that the following items are present in the relevant location (e.g. figure legend, table legend, main text, or Methods section).

n/a	Confirmed	
☐	☒	The exact sample size (*n*) for each experimental group/condition, given as a discrete number and unit of measurement
☐	☒	An indication of whether measurements were taken from distinct samples or whether the same sample was measured repeatedly
☒	☐	The statistical test(s) used AND whether they are one- or two-sided *Only common tests should be described solely by name; describe more complex techniques in the Methods section.*
☒	☐	A description of all covariates tested
☒	☐	A description of any assumptions or corrections, such as tests of normality and adjustment for multiple comparisons
☐	☒	A full description of the statistics including central tendency (e.g. means) or other basic estimates (e.g. regression coefficient) AND variation (e.g. standard deviation) or associated estimates of uncertainty (e.g. confidence intervals)
☒	☐	For null hypothesis testing, the test statistic (e.g. *F*, *t*, *r*) with confidence intervals, effect sizes, degrees of freedom and *P* value noted *Give P values as exact values whenever suitable.*
☒	☐	For Bayesian analysis, information on the choice of priors and Markov chain Monte Carlo settings
☒	☐	For hierarchical and complex designs, identification of the appropriate level for tests and full reporting of outcomes
☒	☐	Estimates of effect sizes (e.g. Cohen's *d*, Pearson's *r*), indicating how they were calculated
☐	☒	Clearly defined error bars *State explicitly what error bars represent (e.g. SD, SE, CI)*

Our web collection on statistics for biologists may be useful.

Software and code

Policy information about availability of computer code

Data collection	FEI EPU 1.9 , SerialEM 3.6, Clampfit 10
Data analysis	MotionCor2, Gautomatch 0.53, GCTF 1.18, Focus 1.0, Relion 2.1, Chimera 1.8.1, Pymol 1.7, HOLE 2.11, ccp4 7, phenix 1.14, Coot 0.8.8, NAMD 2.12, VMD 1.9.3, Molprobity 4.3, CueMol 2.2.3, Axograph 1.7, pClamp 10.3, Prism 5, KaleidaGraph 3.6

For manuscripts utilizing custom algorithms or software that are central to the research but not yet described in published literature, software must be made available to editors/reviewers upon request. We strongly encourage code deposition in a community repository (e.g. GitHub). See the Nature Research guidelines for submitting code & software for further information.

Data

Policy information about availability of data

All manuscripts must include a data availability statement. This statement should provide the following information, where applicable:

- Accession codes, unique identifiers, or web links for publicly available datasets
- A list of figures that have associated raw data
- A description of any restrictions on data availability

Atomic coordinates of the four conformations have been deposited in the Protein Data Bank with accession number XXXX, XXXX, XXXX, XXXX for conformations T, I1,

F and I2 respectively. The cryo-EM density maps have been deposited in the Electron Microscopy Data Bank with accession number XXXX, XXXX, XXXX, XXXX for conformations T, I1, F and I2 respectively.

Field-specific reporting

Please select the best fit for your research. If you are not sure, read the appropriate sections before making your selection.

☒ Life sciences   ☐ Behavioural & social sciences   ☐ Ecological, evolutionary & environmental sciences

For a reference copy of the document with all sections, see nature.com/authors/policies/ReportingSummary-flat.pdf

Life sciences study design

All studies must disclose on these points even when the disclosure is negative.

Sample size	N/A
Data exclusions	No data was excluded from the analysis
Replication	All attemps to replicate the data were successful
Randomization	N/A
Blinding	N/A

Reporting for specific materials, systems and methods

Materials & experimental systems

n/a	Involved in the study
☐	☒ Unique biological materials
☒	☐ Antibodies
☐	☒ Eukaryotic cell lines
☒	☐ Palaeontology
☒	☐ Animals and other organisms
☒	☐ Human research participants

Methods

n/a	Involved in the study
☒	☐ ChIP-seq
☒	☐ Flow cytometry
☒	☐ MRI-based neuroimaging

Unique biological materials

Policy information about availability of materials

Obtaining unique materials | No restrictions. Plasmids or cells can be requested by email to the corresponding authors.

Eukaryotic cell lines

Policy information about cell lines

Cell line source(s)	A HEK T-rex (Thermo Fisher) derived cell line was used. It was modify to express the m5HT3A receptor under control of tetracycline
Authentication	No method for authentication was used
Mycoplasma contamination	No mycoplasma contamination test was performed
Commonly misidentified lines (See ICLAC register)	N/A